High Order Still-Water and Moving-Water Equilibria Preserving Discontinuous Galerkin Methods for the Ripa Model

Jolene Britton[1] · Yulong Xing[2]

Abstract

Shallow water equations with horizontal temperature gradients, also known as the Ripa system, are used to model flows when the temperature fluctuations play an important role. These equations admit steady state solutions where the fluxes and source terms balance each other. We present well-balanced discontinuous Galerkin methods for the Ripa model which can preserve the still-water or the general moving-water equilibria. The key ideas are the recovery of well-balanced states, separation of the solution into the equilibrium and fluctuation components, and appropriate approximations of the numerical fluxes and source terms. The same framework is also extended to design well-balanced methods for the constant height and isobaric steady state solutions of the Ripa model. Numerical examples are presented to verify the well-balanced property, high order accuracy, and good resolution for both smooth and discontinuous solutions.

Keywords Discontinuous Galerkin methods · Well-balanced methods · Ripa model · Shallow water equations · Moving-water equilibrium

1 Introduction

The shallow water equations with temperature fluctuations were introduced by Ripa in 1993 [11,22,23]. These equations are often referred to as the Ripa system and were introduced for the purpose of modeling ocean currents. The introduction of temperature is advantageous because the movement and behavior of ocean currents are impacted by forces such as temperature acting upon the water. The one-dimensional Ripa equations take the form:

✉ Yulong Xing
    xing.205@osu.edu

    Jolene Britton
    jhout001@ucr.edu

1   Department of Mathematics, University of California Riverside, Riverside, CA 92521, USA

2   Department of Mathematics, Ohio State University, Columbus, OH 43210, USA

$$\begin{cases} h_t + (hu)_x = 0, \\ (hu)_t + (hu^2 + \frac{1}{2}gh^2\theta)_x = -gh\theta b_x, \\ (h\theta)_t + (h\theta u)_x = 0, \end{cases} \tag{1.1}$$

where $h(x,t) \geq 0$ represents the height of the water, $u(x,t) \in \mathbb{R}$ describes the velocity, $\theta(x,t) > 0$ is a potential temperature field, $b(x)$ represents the bottom topography, and g is the gravitational constant. The term hu represents water discharge and $gh^2\theta/2$ is the pressure depending on the water temperature. The potential temperature field θ is defined to be the reduced gravity $g\Delta\Theta/\Theta_{\text{ref}}$ [9], where $\Delta\Theta$ is set to be the difference in potential temperature from a reference value Θ_{ref}. Additional source terms that model the friction along the bottom and surface or variations in the width of the channel could be included. In this paper, we only consider the source term that accounts for the bottom topography.

The Ripa system is a generalized model of the shallow water equations. The one-dimensional shallow water equations take the form:

$$\begin{cases} h_t + (hu)_x = 0, \\ (hu)_t + (hu^2 + \frac{1}{2}gh^2)_x = -ghb_x. \end{cases} \tag{1.2}$$

Notice that, when the potential temperature field $\theta = 1$ in the Ripa model (1.1), the shallow water equations (1.2) are recovered. The shallow water equations consist of the conservation of mass and momentum, with the assumption that the density is constant. Two-layer and multi-layer shallow water equations [4] have been studied to model the flows in the shallow water regime where several layers with different densities appear. Such a model assumes a piecewise constant density inside each layer, and allows for different densities across the layers. Challenges in studying such models arise from the complicated eigenstructure, non-conservative terms, and conditional hyperbolicity, etc. Despite these challenges, there have been many studies on various numerical methods for multi-layer shallow water equations. The Ripa model can be obtained by vertically averaging each variable (including the density) over all layers from the bottom to the top, therefore, we lose the information of the interface between layers, but the resulting model has a simpler eigenstructure and is always hyperbolic in the conservative form. The horizontal temperature gradients are introduced in the Ripa model to represent the variations in the fluid density.

Both the Ripa system (1.1) and the shallow water equations (1.2) belong to the family of hyperbolic balance laws, which have gained growing attention in the last few decades. In the one dimensional setting, such models usually take the form of

$$U_t + F(U)_x = S(U).$$

Due to the existence of the source term $S(U)$, hyperbolic balance laws introduce new computational challenges beyond the existing challenges of hyperbolic conservation laws. Balance laws often admit non-trivial steady state solutions in which the source term balances the effect of the flux gradients. The balance of fluxes and the source term as well as small perturbations of steady state solutions cannot be captured well by standard numerical methods with a straightforward implementation of the source term, unless a much refined mesh is used. Therefore, well-balanced methods, which can exactly preserve steady state solution at the discrete level, are introduced to provide an accurate solution on a relatively coarse mesh and resolve small perturbations to steady state solutions accurately.

The steady state solutions of the Ripa model (1.1) occur when $\partial_t U = 0$, that is

$$\begin{cases} \partial_x(hu) = 0, \\ \partial_x\left(hu^2 + \frac{1}{2}gh^2\theta\right) = -gh\theta b_x, \\ \partial_x(h\theta u) = 0. \end{cases} \tag{1.3}$$

In the case of still-water, when the velocity u is zero, the steady state system (1.3) reduces to

$$\begin{cases} u = 0 \\ \partial_x\left(\frac{1}{2}h^2\theta\right) = -h\theta b_x, \end{cases} \tag{1.4}$$

which is an underdetermined PDE system. In order to reach a solution for (1.4), additional assumptions for h, θ or b must be enforced. There are three cases to consider if we require one of these variables to be constant. This raises one discrepancy between the Ripa model and the shallow water equations. The first case is the *still-water* steady state, which corresponds to a flat water surface under constant temperature:

$$\left(u, \theta, h + b\right) = \left(0, C_1, C_2\right), \tag{1.5}$$

where C_1, C_2 are constants. This is the same lake-at-rest steady state solution of the shallow water equations. The second case is the *isobaric* steady state, which corresponds to a wave in which the height and temperature jump but velocity and pressure remain constant:

$$\left(u, b, h^2\theta\right) = \left(0, C_1, C_2\right). \tag{1.6}$$

The last case is the *constant water height* steady state:

$$\left(u, h, b + \frac{1}{2}h\ln\theta\right) = \left(0, C_1, C_2\right). \tag{1.7}$$

The more general case occurs when the velocity u does not vanish. The *moving-water* equilibrium is given by:

$$\begin{cases} hu = constant, \\ \theta = constant, \\ \frac{u^2}{2} + g\theta(h + b) = constant, \end{cases} \tag{1.8}$$

where the momentum hu and potential temperature field θ are constant. It is easy to observe that the lake-at-rest still-water steady state (1.5) is simply a special case of the moving-water steady state (1.8). Well-balanced methods for the moving-water equilibrium can automatically preserve the lake-at-rest steady state, but not vice versa.

Well-balanced numerical methods for shallow water equations are far more studied in the literature, and can serve as a foundation of well-balanced methods for Ripa models. A vast amount of well-balanced methods for the still-water steady state [1,2,16,17,21,31] have been studied, and we refer to the survey papers [15,34] for a complete list of existing literature on this topic. Well-balanced methods for the moving-water equilibrium are more complicated and it is much more difficult to design such methods. Comparison of well-balanced methods for the still-water and moving-water steady state solutions has been provided in [35], where some numerical examples are shown to demonstrate the advantage of moving-water well-balanced methods, especially for solutions near a moving-water equilibrium. Some moving-water well-balanced methods been proposed in [3,7,8,24], and high order accurate well-balanced weighted essentially non-oscillatory (WENO) methods can be found in [5,19,25].

In [30], well-balanced and positivity-preserving discontinuous Galerkin (DG) methods were developed for the shallow water equations with moving-water equilibrium.

Designing well-balanced methods for the Ripa model (1.1) can be a challenging task, because its steady states are more complicated than those of the shallow water equations [9]. In the last few years, there have been some studies on well-balanced methods for the Ripa models, mostly focusing on the zero-velocity steady-state solutions (1.5) and (1.6). The first well-balanced scheme for the Ripa system is developed in [9]. The proposed scheme is well-balanced, positivity preserving and does not develop spurious pressure oscillations in the neighborhood of temperature jumps. A second-order well-balanced finite volume scheme for the Ripa system in one and two dimensions is designed in [28]. High-order well-balanced WENO schemes that possess sharp shock transition were designed for the Ripa system in [13], by extending the well-balanced technique developed in [31] for the shallow water equations. Other related works can be found in [12,14,26].

High order accurate numerical schemes such as finite difference and finite volume WENO schemes, spectral methods, and DG methods have been developed to reduce the number of computational cells and thus reduce the computational time, while still achieving high order accuracy. Specifically, the DG method is a class of finite element methods in which the numerical solutions and test functions live in a discontinuous piecewise polynomial space. A review of the method can be found in [10]. The DG method combines the flexibility of the finite element method and the stability of the finite volume method. Additionally, DG methods enjoy advantages including high order accuracy, high parallel efficiency, flexibility for hp-adaptivity and arbitrary geometry and meshes, etc.

The main objective of this paper is to develop high order well-balanced DG methods for the Ripa system (1.1), which can preserve the still-water equilibrium solution (1.5) and moving-water steady state solution (1.8) exactly at the discrete level. This will be the first moving-water well-balanced method for the Ripa model, to our best knowledge. To achieve this goal, we start with a transformation between the conservative variables and the equilibrium variables (to be defined in Sect. 4). For the finite element methods, the initial conditions are projected into a polynomial solution spaces to provide a numerical initial condition. Even though the exact initial conditions are in moving-water equilibrium, the numerical initial conditions may no longer be. One challenge in designing well-balanced methods is the recovery of the well-balanced states from the numerical initial condition, which is achieved by a new choice of projection operator. Then, we can decompose the numerical solution into an equilibrium part and the fluctuation part, and show that the fluctuation part is zero at the steady state. Following the idea of hydrostatic reconstruction, one can carefully design well-balanced numerical fluxes. A well-balanced source term approximation is achieved by treating the equilibrium and fluctuation parts in different ways.

The methods presented here are extensions of the ones in [30] for the moving-water equilibrium of the shallow water equations. In this paper, several improvements over the well-balanced methods in [30] have been presented to improve the algorithm. First, the recovery of the well-balanced states in [30] are obtained by solving nonlinear equations, which could be complicated. A special projection of the exact initial condition is proposed in this paper in order to provide a much easier way to recover the well-balanced states. This also leads to a more simple way to evaluate the well-balanced components of the solutions at each time step. Second, due to the existence of the potential temperature field, extra attention is provided to accommodate more components in the conservative and the equilibrium variables. Lastly, we simplify the procedure to evaluate the updated cell boundary values resulted from the hydrostatic reconstruction. This leads to a more efficient and simple way to compute the well-balanced numerical fluxes than those computed in [30]. Furthermore, the same idea

can be generalized to preserve other steady state solutions of the Ripa system, including the isobaric and constant water height equilibria which do not appear in the shallow water equations.

This paper is organized as follows. In Sect. 2, we introduce some notations and discuss the well-balanced DG method for still-water lake-at-rest equilibrium. Numerical examples using the methods outlined in Sect. 2 are found in Sect. 3 to demonstrate the accuracy and well-balanced property of the scheme as well as show that it can aptly handle perturbations of the still-water steady state and provide good resolution for discontinuous solutions. Although our main focus is on moving-water well-balanced methods, it is useful to present the still-water preserving DG methods in Sects. 2 and 3. The purpose is twofold. First, the well-balanced DG method for still-water equilibrium is not available in the literature and a simple method achieving such a goal is interesting by itself. Second, this would serve as a basis for the design of the moving-water well-balanced methods for the Ripa system, which is presented in Sect. 4. We will also show that when applied to still-water equilibrium, the proposed moving-water well-balanced methods reduce to the still-water well-balanced method in Sect. 2. Additionally, we show how the method can be modified to preserve the constant water height and isobaric steady states. In Sect. 5, numerical examples of our methods for the one-dimensional Ripa system are provided, to demonstrate the high order accuracy, well-balanced property, and good resolution for smooth and discontinuous solutions. Finally, concluding remarks are contained in Sect. 6.

2 Still-Water Well-Balanced DG Methods

A variety of well-balanced DG methods for the shallow water equations with still-water steady state solutions

$$u = 0, \quad h + b = \text{constant} \tag{2.1}$$

have been developed. In this section, we extend the method introduced in [33,36] to provide still-water well-balanced methods for the Ripa system (1.1), with the still-water steady state solution (1.5). The same structure will be generalized in Sect. 4 for the moving-water case. The still-water well-balanced DG methods are much simpler than the moving-water well-balanced methods, and would be useful if one's target is to simulate a small perturbation of the still-water equilibrium state. The still-water well-balanced method presented can be extended to two-dimensional Ripa models easily. However, there is no general form of the moving-water equilibrium in two dimensions, hence no two-dimensional moving-water well-balanced methods are available.

2.1 Notation and DG Numerical Scheme

In order to shorten notation, we rewrite (1.1) as

$$\partial_t U + \partial_x f(U) = S(U, b), \tag{2.2}$$

where

$$U = \begin{pmatrix} h \\ hu \\ h\theta \end{pmatrix}, \quad f(U) = \begin{pmatrix} hu \\ hu^2 + \frac{1}{2}gh^2\theta \\ h\theta u \end{pmatrix}, \quad S(U, b) = \begin{pmatrix} 0 \\ -gh\theta b_x \\ 0 \end{pmatrix}. \tag{2.3}$$

The variables U are the conservative variables, $f(U)$ is the flux, and $S(U, b)$ is the source term.

We discretize the computational domain into cells $I_j = [x_{j-\frac{1}{2}}, x_{j+\frac{1}{2}}]$, and denote the size of the jth cell by Δx_j. Furthermore, we let $\tau = \max_j \Delta x_j$. We seek an approximation U_τ which belongs to the finite dimensional DG space:

$$\mathbb{V}_\tau^k = \{v : v|_{I_j} \in P^k(I_j), j = 1, \ldots, J\}, \tag{2.4}$$

where $P^k(I)$ is the space of polynomials of degree up to k in the domain I, and J is the total number of cells. In addition, b_τ denotes the projection of the bottom function b into $\mathbb{V}_\tau^k$. We denote $U_{\tau,j+\frac{1}{2}}^+$ and $U_{\tau,j+\frac{1}{2}}^-$ as the limit values of U_τ at the element interface $x_{j+\frac{1}{2}}$ from the right cell I_{j+1} and from the left cell I_j, respectively. The conventional DG scheme in each cell can be formulated as

$$\int_{I_j} \partial_t U_\tau v \, dx - \int_{I_j} f(U_\tau) \partial_x v \, dx + \hat{f}_{j+\frac{1}{2}} v_{j+\frac{1}{2}}^- - \hat{f}_{j-\frac{1}{2}} v_{j-\frac{1}{2}}^+ = \int_{I_j} S(U_\tau, b_\tau) v \, dx, \tag{2.5}$$

where $v(x)$ is a test function from the test space $\mathbb{V}_\tau^k$ and

$$\hat{f}_{j+\frac{1}{2}} = F\left(U_\tau\left(x_{j+\frac{1}{2}}^-, t\right), U_\tau\left(x_{j-\frac{1}{2}}^+, t\right)\right),$$

with $F(a, b)$ being the numerical flux. It has been shown that for high order DG methods, the effect of different fluxes on the accuracy of methods is relatively small [20]. Therefore, in this paper, we will employ the use of the simple Lax–Friedrichs flux:

$$F(a, b) = \frac{1}{2}\left(f(a) + f(b) - \alpha(b - a)\right), \tag{2.6}$$

where $\alpha = \max(|u| + \sqrt{gh\theta})$, and the maximum in the calculation of α is taken either globally (Lax–Friedrichs flux) or locally (local Lax–Friedrichs flux).

We aim to preserve the lake-at-rest still-water solution (1.5). The well-balanced numerical scheme, as described in [36] for the shallow water equations, has the form:

$$\int_{I_j} \partial_t U_\tau^n v \, dx - \int_{I_j} f(U_\tau^n) \partial_x v \, dx + \hat{f}_{j+\frac{1}{2}}^l v_{j+\frac{1}{2}}^- - \hat{f}_{j-\frac{1}{2}}^r v_{j-\frac{1}{2}}^+ = \int_{I_j} S(U_\tau^n, b_\tau) v \, dx \tag{2.7}$$

The design of $\hat{f}_{j+\frac{1}{2}}^l$ and $\hat{f}_{j-\frac{1}{2}}^r$, known as the well-balanced numerical fluxes, are defined below in Sect. 2.2. The source term approximation will be discussed in Sect. 2.3. This method is equivalent to

$$\int_{I_j} \partial_t U_\tau^n v \, dx - \int_{I_j} f(U_\tau^n) \partial_x v \, dx + \hat{f}_{j+\frac{1}{2}} v_{j+\frac{1}{2}}^- - \hat{f}_{j-\frac{1}{2}} v_{j-\frac{1}{2}}^+$$
$$= \int_{I_j} S(U_\tau^n, b_\tau) v \, dx + \left(\hat{f}_{j+\frac{1}{2}} - \hat{f}_{j+\frac{1}{2}}^l\right) v_{j+\frac{1}{2}}^- - \left(\hat{f}_{j-\frac{1}{2}} - \hat{f}_{j-\frac{1}{2}}^r\right) v_{j-\frac{1}{2}}^+, \tag{2.8}$$

and the terms $\hat{f}_{j+\frac{1}{2}} - \hat{f}_{j+\frac{1}{2}}^l$ and $\hat{f}_{j-\frac{1}{2}} - \hat{f}_{j-\frac{1}{2}}^r$ are at the level of $O(\tau^{k+1})$ (independent of the smoothness of the solution U) when the bottom topography b is smooth, and can be viewed as high order correction terms to the source term approximation.

The total variation diminishing (TVD) Runge–Kutta time discretization is used to increase temporal accuracy and stability. The third order TVD Runge–Kutta method, described as:

$$
\begin{aligned}
U_\tau^{(1)} &= U_\tau^n + \Delta t \mathcal{F}(U_\tau^n), \\
U_\tau^{(2)} &= \frac{3}{4} U_\tau^n + \frac{1}{4}\left(U_\tau^{(1)} + \Delta t \mathcal{F}\left(U_\tau^{(1)}\right)\right), \\
U_\tau^{n+1} &= \frac{1}{3} U_\tau^n + \frac{2}{3}\left(U_\tau^{(2)} + \Delta t \mathcal{F}\left(U_\tau^{(2)}\right)\right),
\end{aligned}
\tag{2.9}
$$

is used throughout this paper, where $\mathcal{F}$ is the spatial operator. In the following subsections we describe how the flux functions are defined and the source term is decomposed.

2.2 Well-Balanced Numerical Fluxes

The conservative variable can be decomposed into a reference equilibrium state U_τ^e and a fluctuation part U_τ^f. In each computational cell I_j, the equilibrium state $U_\tau^e(x)$ can be computed from the constant equilibrium variables defined as (setting $H = h + b$)

$$
\hat{V}_j = \begin{pmatrix} \hat{H}_j \\ \hat{m}_j \\ \hat{\theta}_j \end{pmatrix} = \begin{pmatrix} (h_\tau + b_\tau)\left(x_{j+\frac{1}{2}}^-\right) \\ (hu)_\tau\left(x_{j+\frac{1}{2}}^-\right) \\ \theta_\tau\left(x_{j+\frac{1}{2}}^-\right) \end{pmatrix},
\tag{2.10}
$$

and the bottom function b_τ in the form of

$$
U_{\tau,j}^e(x) = \begin{pmatrix} h_{\tau,j}^e(x) \\ (hu)_{\tau,j}^e(x) \\ (h\theta)_{\tau,j}^e(x) \end{pmatrix} = \begin{pmatrix} \hat{H}_j - b_\tau(x) \\ \hat{m}_j \\ \left(\hat{H}_j - b_\tau(x)\right)\hat{\theta}_j \end{pmatrix},
\tag{2.11}
$$

which belongs to the DG space $\mathbb{V}_\tau^k$. The fluctuation part U_τ^f is then determined by the decomposition

$$
U_\tau = U_\tau^e + U_\tau^f.
\tag{2.12}
$$

It is easy to observe that at the still-water steady state (1.5), the reference equilibrium state U_τ^e is equal to U_τ, and U_τ^f reduces to 0.

The numerical fluxes are constructed following the approaches in [33,36]. After computing the boundary values $U_{\tau,j+\frac{1}{2}}^\pm$ at the time step t^n, we set

$$
b_{\tau,j+\frac{1}{2}}^* = \max\left(b_{\tau,j+\frac{1}{2}}^+, b_{\tau,j+\frac{1}{2}}^-\right),
\tag{2.13}
$$

by utilizing the idea of hydrostatic reconstruction in [1]. A new hydrostatic reconstruction method has been presented in [6], which performs better in some cases, for example, when water runs down a hill. Next, the height function at the cell interface can be redefined as:

$$
h_{\tau,j+\frac{1}{2}}^{*,\pm} = \max\left(0, h_{\tau,j+\frac{1}{2}}^\pm + b_{\tau,j+\frac{1}{2}}^\pm - b_{j+\frac{1}{2}}^*\right),
\tag{2.14}
$$

or equivalently,

$$
\begin{aligned}
h^{*,-}_{\tau,j+\frac{1}{2}} &= \max\left(0, \hat{H}_j - b^*_{\tau,j+\frac{1}{2}} + (h^f)^-_{\tau,j+\frac{1}{2}}\right), \\
h^{*,+}_{\tau,j+\frac{1}{2}} &= \max\left(0, \hat{H}_{j+1} - b^*_{\tau,j+\frac{1}{2}} + (h^f)^+_{\tau,j+\frac{1}{2}}\right),
\end{aligned}
\tag{2.15}
$$

by using the new defined $\hat{H}_j$ and h^f. This results in the following updated boundary values of U:

$$
U^{*,\pm}_{\tau,j+\frac{1}{2}} = \begin{pmatrix} h^{*,\pm}_{\tau,j+\frac{1}{2}} \\ h^{*,\pm}_{\tau,j+\frac{1}{2}} u^{\pm}_{\tau,j+\frac{1}{2}} \\ h^{*,\pm}_{\tau,j+\frac{1}{2}} \theta^{\pm}_{\tau,j+\frac{1}{2}} \end{pmatrix}.
\tag{2.16}
$$

Finally, the left and right fluxes are given as:

$$
\begin{aligned}
\hat{f}^l_{j+\frac{1}{2}} &= F\left(U^{*,-}_{\tau,j+\frac{1}{2}}, U^{*,+}_{\tau,j+\frac{1}{2}}\right) + f\left(U^-_{\tau,j+\frac{1}{2}}\right) - f\left(U^{*,-}_{\tau,j+\frac{1}{2}}\right), \\
\hat{f}^r_{j-\frac{1}{2}} &= F\left(U^{*,-}_{\tau,j-\frac{1}{2}}, U^{*,+}_{\tau,j-\frac{1}{2}}\right) + f\left(U^+_{\tau,j-\frac{1}{2}}\right) - f\left(U^{*,+}_{\tau,j-\frac{1}{2}}\right).
\end{aligned}
\tag{2.17}
$$

At the steady state (1.5), although the original cell boundary values $h^+_{\tau,j+\frac{1}{2}}, h^-_{\tau,j+\frac{1}{2}}$ may not be the same, we have $h^{\pm}_{\tau,j+\frac{1}{2}} + b^{\pm}_{\tau,j+\frac{1}{2}} = constant$. Then following the definition in (2.14), this implies $h^{*,+}_{\tau,j+\frac{1}{2}} = h^{*,-}_{\tau,j+\frac{1}{2}}$. Since $u^{\pm}_{\tau,j+\frac{1}{2}} = 0$ and $\theta^{\pm}_{\tau,j+\frac{1}{2}} = constant$ at the steady state (1.5), we can conclude that U^*_τ is continuous at cell interfaces, i.e. $U^{*,+}_{\tau,j+\frac{1}{2}} = U^{*,-}_{\tau,j+\frac{1}{2}}$. Furthermore, due to the consistency of the numerical flux F, it can be shown that $\hat{f}^l_{j+\frac{1}{2}} = f\left(U^-_{\tau,j+\frac{1}{2}}\right)$ and $\hat{f}^r_{j-\frac{1}{2}} = f\left(U^+_{\tau,j-\frac{1}{2}}\right)$, which is a desirable quality for achieving the well-balanced property.

2.3 The Source Term Decomposition

The source term can be decomposed similarly as in (2.12), because $S(U,b) = -gh\theta b_x$ is linear with respect to the conservative variable $h\theta$:

$$
\int_{I_j} S(U_\tau, b_\tau) v \, dx = \int_{I_j} S(U^e_\tau, b_\tau) v \, dx + \int_{I_j} S(U^f_\tau, b_\tau) v \, dx.
\tag{2.18}
$$

Notice that the second term on the right hand side can be directly computed by any quadrature rule with sufficient accuracy. On the other hand, since $U^e_{\tau,j}(x)$ is the equilibrium state, the first term on the right hand side can be expanded as

$$
\int_{I_j} S\left(U^e_\tau, b_\tau\right) v \, dx = - \int_{I_j} f\left(U^e_\tau\right) v_x \, dx + f\left(U^{e,-}_{\tau,j+\frac{1}{2}}\right) v^-_{j+\frac{1}{2}} - f\left(U^{e,+}_{\tau,j-\frac{1}{2}}\right) v^+_{j-\frac{1}{2}},
\tag{2.19}
$$

where $U^e_\tau \in \mathbb{V}^k_\tau$ is a polynomial. On the numerical level, when all these integrals are replaced by numerical integrations, this equality holds exactly if one uses a quadrature rule which is accurate for polynomial of degree $3k - 1$. If a less accurate quadrature rule is used, the equality holds approximately, up to the accuracy of the quadrature rule. Thus the source term

can be evaluated using the following form:

$$\int_{I_j} S\left(U_\tau, b_\tau\right) v \, dx = -\int_{I_j} f\left(U_\tau^e\right) v_x \, dx + f\left(U_{\tau,j+\frac{1}{2}}^{e,-}\right) v_{j+\frac{1}{2}}^- - f\left(U_{\tau,j-\frac{1}{2}}^{e,+}\right) v_{j-\frac{1}{2}}^+$$
$$+ \int_{I_j} S\left(U_\tau^f, b_\tau\right) v \, dx. \tag{2.20}$$

Since the only non-zero source term is in the momentum equation, we can plug in the definition of the flux and U_τ^e to obtain the following equivalent source term approximation

$$\begin{aligned}
-\int_{I_j} gh_\tau \theta_\tau (b_\tau)_x v \, dx &= \frac{1}{2} g\hat{\theta}_j\left(\left(\hat{H}_j - b_\tau\right)^2 v\right)_{j+\frac{1}{2}}^- - \frac{1}{2} g\hat{\theta}_j\left(\left(\hat{H}_j - b_\tau\right)^2 v\right)_{j-\frac{1}{2}}^+ \\
&\quad - \int_{I_j} \frac{1}{2} g\hat{\theta}_j\left(\hat{H}_j - b_\tau\right)^2 v_x \, dx \\
&\quad - \int_{I_j} g\left(h_\tau \theta_\tau + (\hat{H}_j - b_\tau)\hat{\theta}_j\right)(b_\tau)_x v \, dx \\
&= g\hat{\theta}_j\left(\frac{b_\tau^2}{2} v - \hat{H}_j b_\tau v\right)_{j+\frac{1}{2}}^- - g\theta\left(\frac{b_\tau^2}{2} v - \hat{H}_j b_\tau v\right)_{j-\frac{1}{2}}^+ \\
&\quad - \int_{I_j} g\hat{\theta}_j\left(\frac{b_\tau^2}{2} - \hat{H}_j b_\tau\right) v_x \, dx \\
&\quad - \int_{I_j} g\left(h_\tau \theta_\tau + (\hat{H}_j - b_\tau)\hat{\theta}_j\right)(b_\tau)_x v \, dx.
\end{aligned} \tag{2.21}$$

This formulation is exactly the extension of the source term approximation introduced in [32] for the shallow water equations. However, a different well-balanced approach was used in that paper, where the source term was decomposed as $-ghb_x = -g(h+b)b_x + g(b^2)_x/2$.

Remark 2.1 As we explained, the equality (2.19) holds exactly when a quadrature rule accurate for polynomial of degree $3k - 1$ is used. If this is the case, we can simply replace the source term approximation (2.20) by the direct numerical integration of the source term $-\int_{I_j} gh_\tau \theta_\tau (b_\tau)_x v \, dx$ with this sufficiently high accurate quadrature rule. In other words, the numerical integration of the source term is automatically well-balanced, without any special treatment. The same conclusion has been observed in [33] for the shallow water equations.

Remark 2.2 In this paper, we only consider a source term due to the bottom topography, which is linear with respect to the conservative variable U. When other nonlinear source terms (for instance the Manning friction term) are included, the source term decomposition (2.18) will not hold any more, but one can introduce the following decomposition in a similar manner

$$\int_{I_j} S(U, b)v \, dx = \int_{I_j} S(U^e, b)v \, dx + \int_{I_j} \left(S(U, b) - S(U^e, b)\right) v \, dx. \tag{2.22}$$

Note that when S is linear, i.e., $S(U, b) - S(U^e, b) = S(U - U^e, b) = S(U^f, b)$, this decomposition reduces to (2.18). The first term on the right hand side of (2.22) can be approximated as in (2.19), and the second term on the right hand side is computed by a straightforward numerical integral. This will provide well-balanced source term approximation.

Remark 2.3 When the bottom topography is flat (i.e., $b(x) = constant \ C$), the traditional DG methods are recovered from our well-balanced DG scheme, that is, the source term

approximation reduces to 0 exactly and the left and right numerical fluxes reduce to the original fluxes. First, when $b(x) = C$ is a constant, one has $b_\tau(x) = C$, therefore the source term approximation presented in (2.21) simply reduces to zero. Second, when $b(x) = C$, $b^*_{\tau, j \pm \frac{1}{2}}$ defined in (2.13), is also the same constant, which leads to

$$h^{*,\pm}_{\tau, j+\frac{1}{2}} = \max\left(0, h^\pm_{\tau, j+\frac{1}{2}} + b^\pm_{\tau, j+\frac{1}{2}} - b^*_{j+\frac{1}{2}}\right) = h^\pm_{\tau, j+\frac{1}{2}}.$$

More generally we have $U^{*,\pm}_{\tau, j+\frac{1}{2}} = U^\pm_{\tau, j+\frac{1}{2}}$. Therefore the left and right numerical fluxes defined in (2.17) reduce to the original DG fluxes: $\hat{f}^l_{j+\frac{1}{2}} = \hat{f}_{j+\frac{1}{2}}$, $\hat{f}^r_{j-\frac{1}{2}} = \hat{f}_{j-\frac{1}{2}}$.

At the end of this section, we show that the proposed numerical methods are well-balanced for the still-water steady state solutions.

Proposition 1 *The DG scheme (2.7) for the Ripa system (1.1), paired with the numerical fluxes (2.17) and source term approximation (2.20), is well-balanced for the still-water steady state (1.5).*

One can easily verify this holds by observing that $U^f_\tau = 0$ at the lake-at-rest still-water steady state, and thus the well-balanced numerical fluxes reduce to $\hat{f}^l_{j+\frac{1}{2}} = f\left(U^-_{\tau, j+\frac{1}{2}}\right)$ and $\hat{f}^r_{j-\frac{1}{2}} = f\left(U^+_{\tau, j-\frac{1}{2}}\right)$.

Remark 2.4 Although the description is for one dimensional problem only, the proposed well-balanced methods for the still-water steady state (1.5) can be extended to the two-dimensional problem in a straightforward way.

3 Numerical Tests for the Still-Water Well-Balanced Methods

In this section, we present numerical results of our still-water well-balanced DG methods, described in Sect. 2, for the Ripa system (1.1). Piecewise quadratic polynomials ($k = 2$) in space, paired with the third order TVD Runge–Kutta time discretization (2.9), are used in the tests. The CFL number is taken to be 0.1. The constant M in the TVB limiter is taken to be 0, except for the accuracy test, in which no slope limiter was implemented. The gravitational constant g is fixed to be 9.812 m/s^2. We compute multiple types of tests: an accuracy test, verification of the well-balanced property, small perturbations of steady states, and tests for discontinuous solutions.

3.1 Accuracy Test

In this subsection, we test the accuracy of our still-water well-balanced scheme for smooth solutions. The initial conditions in the domain $x \in [0, 1]$ are given by

$$\begin{cases} h(x, 0) = 5 + e^{\sin(2\pi x)}, \\ (hu)(x, 0) = \sin(\cos(2\pi x)), \\ \theta(x, 0) = \sin(2\pi x) + 2, \end{cases} \tag{3.1}$$

with the bottom function $b(x) = \sin^2(\pi x)$ and periodic boundary conditions. We run the simulation until time 0.02, while the solution is still smooth. Since there is no explicitly
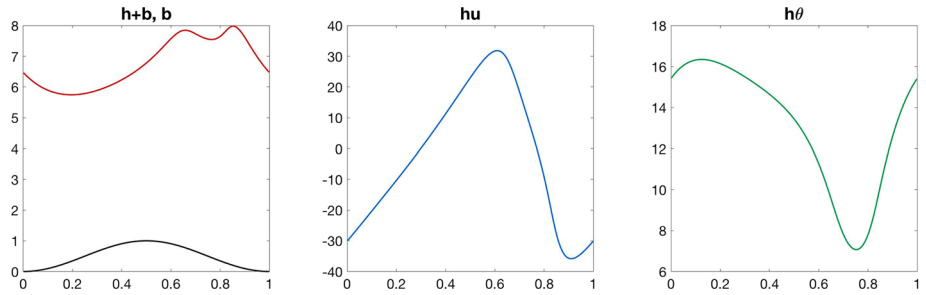
Fig. 1 Solutions of well-balanced methods for the accuracy test in Sect. 3.1 at time $t = 0.02$

Table 1 L^1 errors and orders of accuracy for the test in Sect. 3.1, using the still-water well-balanced method

No. of cells	h		hu		$h\theta$	
	L^1 error	Order	L^1 error	Order	L^1 error	Order
25	0.001347		0.012963		0.001480	
50	0.000205	2.7137	0.001757	2.8829	0.000206	2.8442
100	2.9801e−05	2.7842	0.000226	2.9580	3.2526e−05	2.6638
200	4.0093e−06	2.8939	2.9190e−05	2.9539	5.1699e−06	2.6534
400	5.0280e−07	2.9953	3.6862e−06	2.9852	7.3483e−07	2.8146

known solution in this case, the errors are computed by comparing numerical results of uniform meshes with size J and $2J$. Figure 1 displays the numerical solutions at time 0.02 with 200 uniform cells. Table 1 contains the L^1 errors and numerical orders or accuracy. We can observe that the third order convergence rate is achieved which matches our expectation of order $k + 1$ accuracy.

3.2 Tests for the Well-Balanced Property

The following tests are chosen to verify that the DG methods preserve the still-water steady state (1.3) with a non-flat bottom. For these examples, the errors are calculated by comparing the numerical results to the initial conditions.

First, we will consider the following still-water steady state for $x \in [0, 1]$

$$h + b = 2, \quad u = 0, \quad \theta = 10. \tag{3.2}$$

The bottom function is discontinuous and defined as

$$b(x) = \begin{cases} 1, & \text{if } 0.3 < x < 0.7, \\ 0, & \text{otherwise,} \end{cases}$$

and transmissive boundary conditions are employed. We plot the numerical results at time $t = 1$ with 200 uniform cells in Fig. 2, with the L^1 and L^∞ errors shown in Table 2. From the error table, it can be concluded that the well-balanced property is achieved.

Second, we consider another lake-at-rest still-water steady state problem in which the bottom function defined on the interval domain $[-2, 2]$ consists of two humps and is defined

Table 2 L^1 and L^∞ errors for the well-balanced test to preserve the still-water equilibria

Test	L^1 error			L^∞ error		
	h	hu	$h\theta$	h	hu	$h\theta$
(3.2)	9.9959e−16	7.6925e−15	3.9599e−15	2.6401e−13	4.2333e−12	1.9380e−12
(3.4)	6.9148e−17	1.6519e−15	2.7659e−16	2.8422e−14	4.2056e−12	1.1369e−13
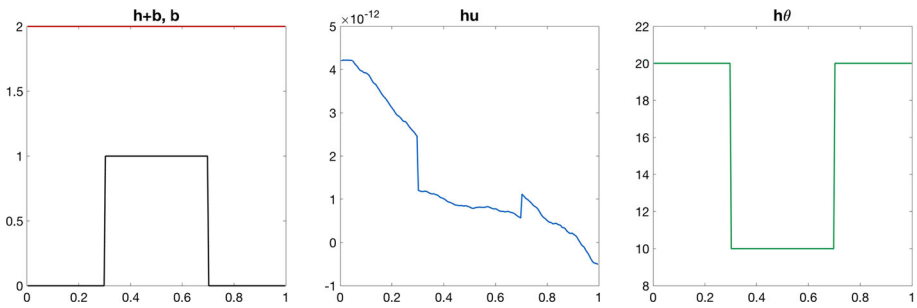
Fig. 2 Solution of well-balanced methods for the still-water steady state problem (3.2) at $t = 1$. The steady state is preserved as $h + b$, hu, and θ are constant

as

$$b(x) = \begin{cases} 0.85(\cos(10\pi(x + 0.9)) + 1), & \text{if } -1 \le x \le -0.8, \\ 1.25(\cos(10\pi(x - 0.4)) + 1), & \text{if } 0.3 \le x \le 0.5, \\ 0, & \text{otherwise.} \end{cases} \tag{3.3}$$

The initial conditions are set as:

$$h(x, 0) = 6 - b(x), \quad u(x, 0) = 0, \quad \theta(x, 0) = 4. \tag{3.4}$$

We run the simulation until time $t = 1$. The numerical results are shown in Fig. 3, and the L^1, L^∞ errors of the numerical solution with 200 uniform cells are presented in Table 2, which shows that the well-balanced property is again maintained. For comparison, we also run the same test with the traditional DG method (i.e., the standard numerical fluxes and the straightforward integration of the source term). The numerical results are presented in Figs. 4 and 5, where we can observe that the steady state is not preserved. It can be seen that, at the region where the bottom function is non-zero, $h + b$ does not preserve the constant steady state, and the solution hu is non-zero.

3.3 Tests of Small Perturbations

The tests in this subsection are selected to demonstrate that perturbations to the still-water steady states are aptly captured by the proposed well-balanced scheme. We will also compare the performance of well-balanced and traditional DG schemes. Prior to defining the perturbations, let us denote χ as the indicator function on an interval:

$$\chi_{[a,b]} = \begin{cases} 1, & \text{if } x \in [a, b], \\ 0, & \text{otherwise,} \end{cases} \tag{3.5}$$
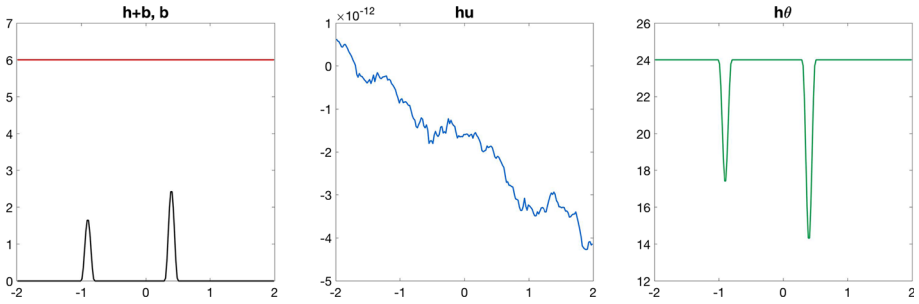
Fig. 3 Solution of well-balanced methods for the still-water steady state flow over two bumps (3.4) at $t = 1$, with 200 uniform cells
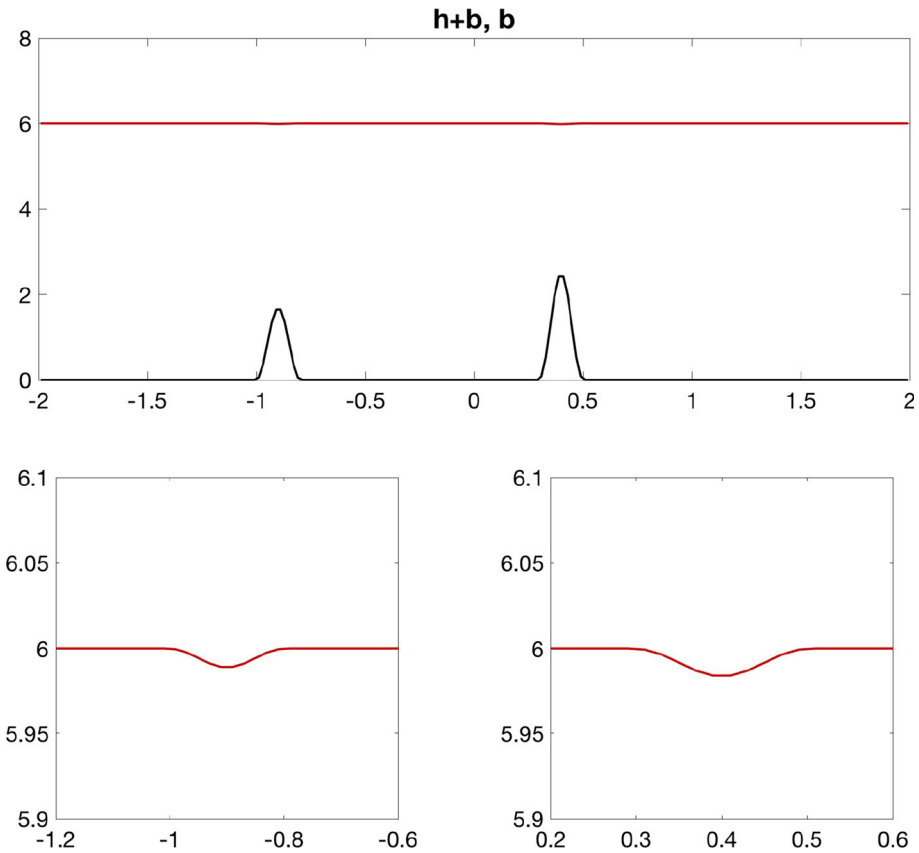
Fig. 4 Solution of non-well-balanced methods for the still-water steady state flow over two bumps (3.4) with 200 uniform cells. It can be seen that the steady state for $h + b$ is not preserved, as the water surface is not flat above the not-constant portions of the bottom function. The bottom figures show zoomed in images of $h + b$ where b is non-constant
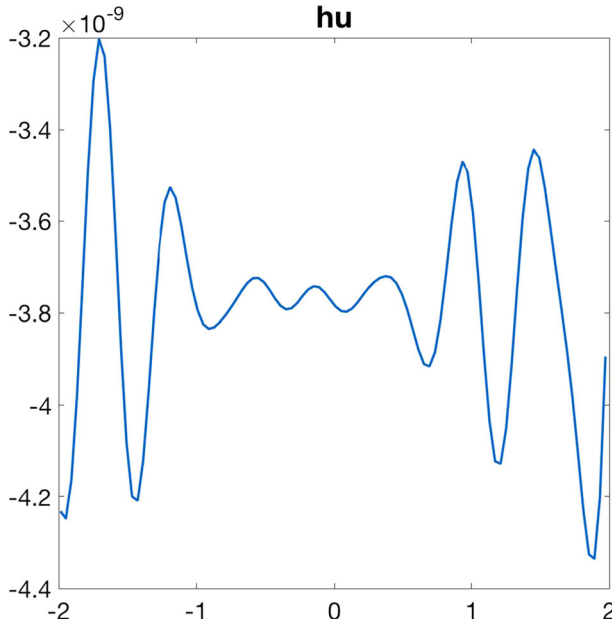
Fig. 5 Solution for hu of the non-well-balanced methods for the still-water steady state flow over two bumps (3.4) with 200 uniform cells. It can be seen that the steady state solution of hu is not preserved as it is non-zero

and denote the still-water steady state initial conditions (3.4) in Sect. 3.2 as $\left(h_{eq}, (hu)_{eq}, (h\theta)_{eq}\right)(x, 0)$. We will examine the numerical results with three different perturbations outlined below.

(a) *Small perturbation to both h and hθ* First, perturbations of sizes $0.01, 0.04$ are applied to the initial conditions of h and $h\theta$, respectively, in the interval $[-1.5, -1.4]$:

$$\left(h, hu, h\theta\right)(x, 0) = \left(h_{eq}, (hu)_{eq}, (h\theta)_{eq}\right)(x, 0) + [0.01, 0, 0.04]\chi_{[-1.5,-1.4]}. \quad (3.6)$$

(b) *Small perturbation to h* Second, a small perturbation of size 0.01 is applied to the initial condition of h in the interval $[-1.5, -1.4]$:

$$\left(h, hu, h\theta\right)(x, 0) = \left(h_{eq}, (hu)_{eq}, (h\theta)_{eq}\right)(x, 0) + [0.01, 0, 0]\chi_{[-1.5,-1.4]}. \quad (3.7)$$

(c) *Large perturbation to h* Third, a larger perturbation of size 1 is applied to the initial condition of h in the interval $[-1.5, -1.4]$:

$$\left(h, hu, h\theta\right)(x, 0) = \left(h_{eq}, (hu)_{eq}, (h\theta)_{eq}\right)(x, 0) + [1, 0, 0]\chi_{[-1.5,-1.4]}. \quad (3.8)$$

The numerical test with the initial condition (3.8) is considered in [9,28] and will be compared to the other tests (3.6), (3.7) in this section. The perturbation of the test (3.6) splits into two waves moving away from the point of origin. On the other hand, the perturbation of the tests (3.7) and (3.8) split into three waves. The two outer waves move away from the point of origin, as expected, while there is a third wave in the center which remains unmoved in the perturbed region. The amplitude of this wave reduces until it reaches a total water height of approximately 6.005 for the test (3.7) and 6.479 for the test (3.8). In the same interval, the value of $h\theta$ converges to a value of approximately 23.980 for the test (3.7) and 22.215
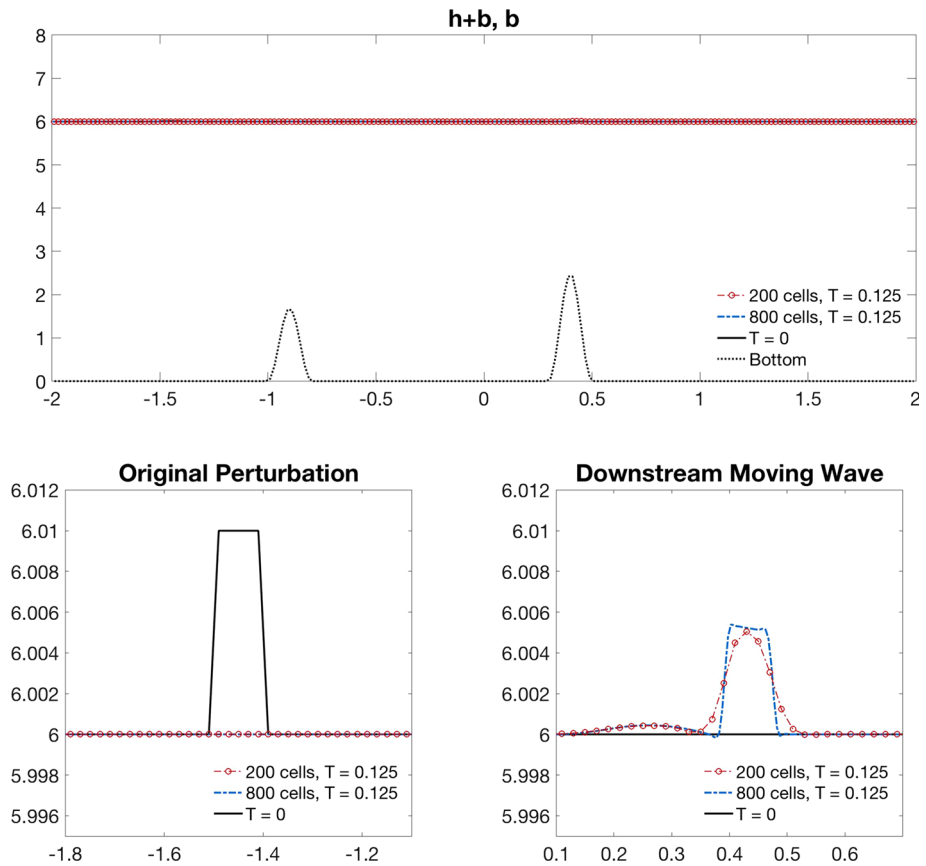
Fig. 6 Initial conditions and numerical solution of water surface $h + b$ for the perturbation tests (3.6), with 200 and 800 uniform cells. The initial perturbation split into two waves moving away from the point of origin. At time $t = 0.125$, the downstream moving wave has passed over the two bumps in the bottom topography and the upstream wave has exited the domain. The bottom left plot contains the original perturbation and the bottom right plot contains a zoomed in image of the remaining downstream moving wave

for the test (3.8). It is easy to verify that, in this region, the solution converges to an isobaric steady state (1.6) as $h^2\theta$ stays constant inside and outside of the interval.

We run the test until time $t = 0.125$. At this point for all perturbation examples, the downstream moving wave has passed through both bumps of the bottom topography function and the upstream moving wave has exited the domain. Figures 6 and 7 compare the numerical results of three perturbation tests for $h + b$ using well-balanced DG methods with mesh sizes of 200 and 800 uniform cells. It can be observed that the solutions are well captured by our methods. Figure 8 compares the results of three cases for hu and $h\theta$. We would like to point out that the solutions contain the isobaric steady state in the interval $[-1.5, -1.4]$ [for examples (3.7) and (3.8)], and our methods perform well for these test cases.

Next we examine the performance of the the traditional DG scheme on the same test cases. Figure 9 includes the numerical results for these tests. It can be seen that the traditional DG scheme does not handle the perturbation as well as the well-balanced scheme. It is especially evident for examples (3.6) and (3.7) in which the initial perturbations were small.
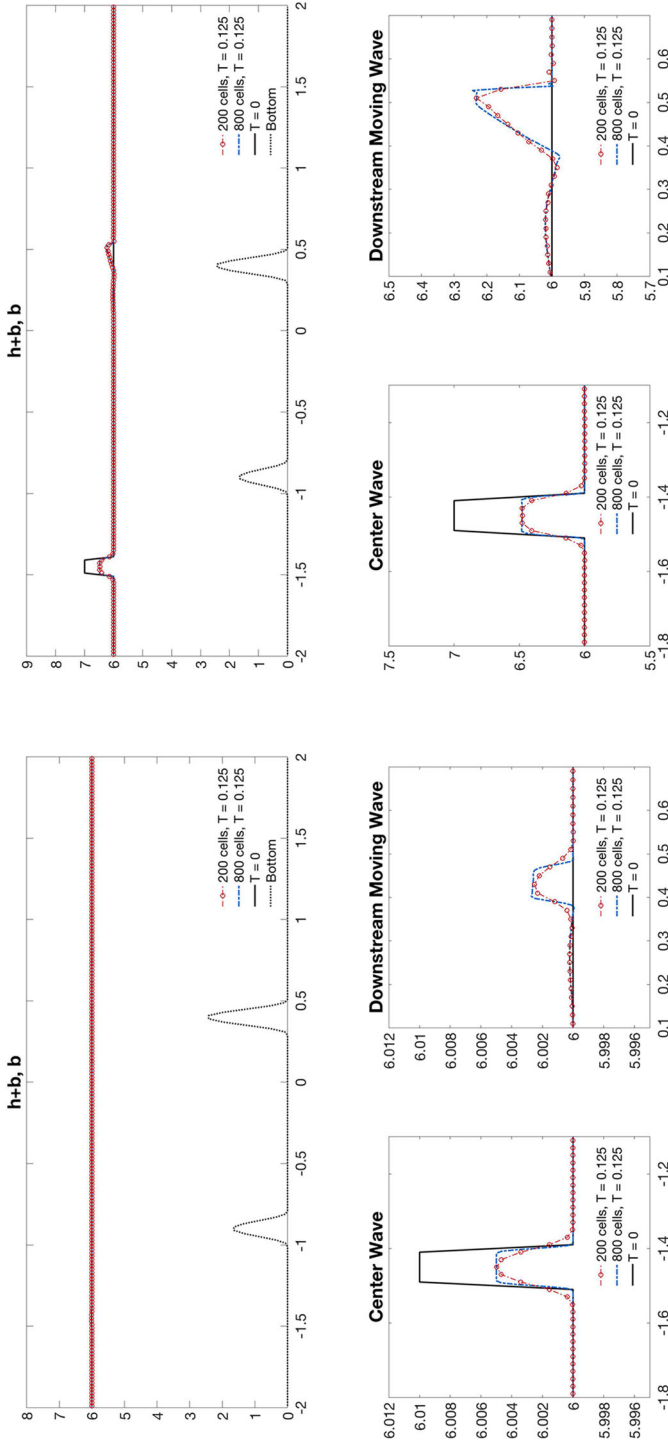
Fig. 7 Initial conditions and numerical solution of water surface $h + b$ for the perturbation tests (3.7) (left plots) and (3.8) (right plots), with 200 and 800 uniform cells. The initial perturbation splits into three waves, one unmoved in the center and the others moving away from the point of origin. At time $t = 0.125$, the downstream moving wave has passed over the two bumps in the bottom topography and the upstream wave has exited the domain. The bottom plots contain zoomed in images of the remaining waves
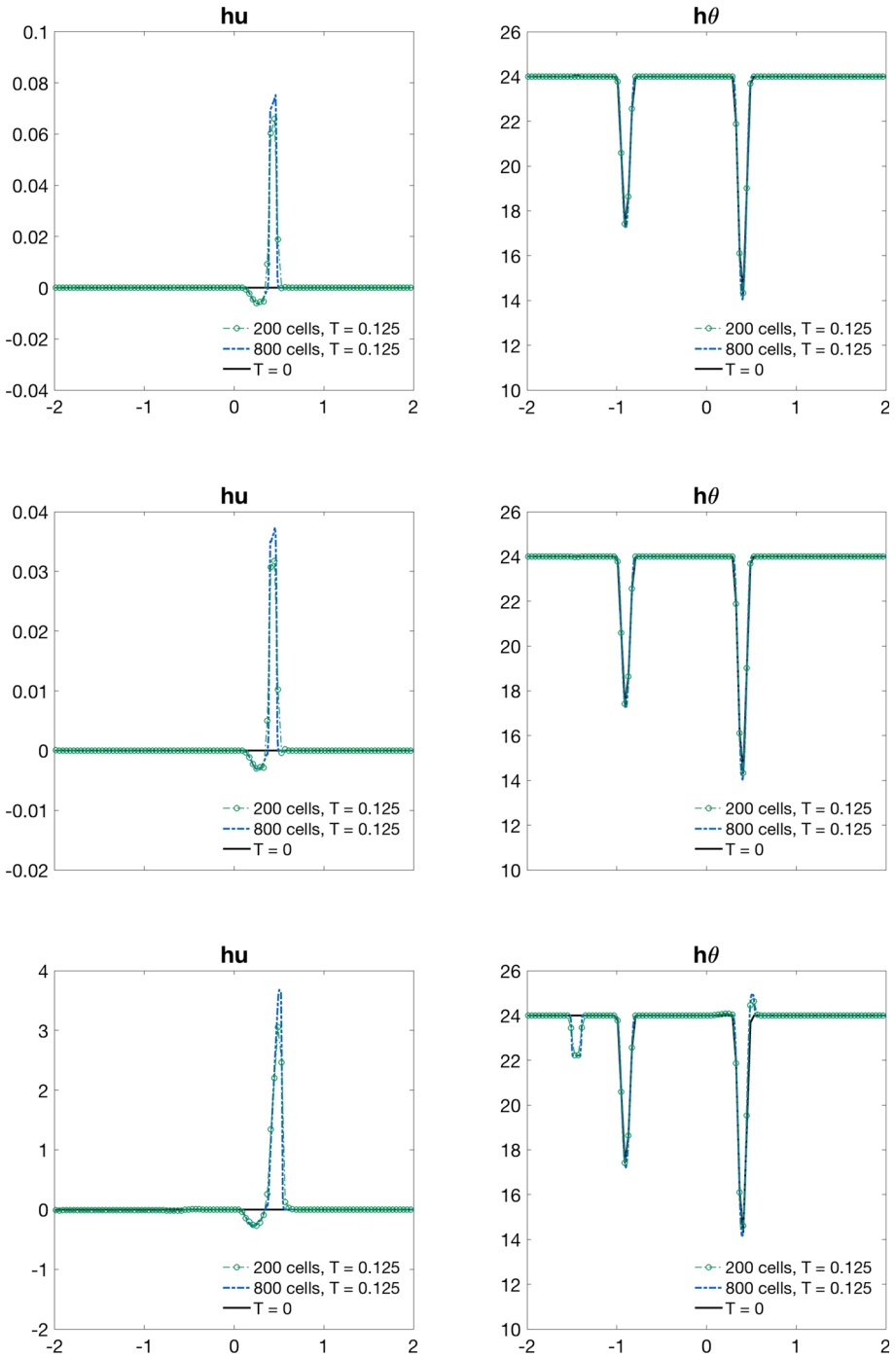
Fig. 8 Initial conditions and numerical solution of $hu, h\theta$ for the perturbation tests (3.6) (top row), (3.7) (middle row), (3.8) (bottom row), with 200 and 800 uniform cells at time $t = 0.125$. Although the shape of hu is similar for all cases, the amplitude varies
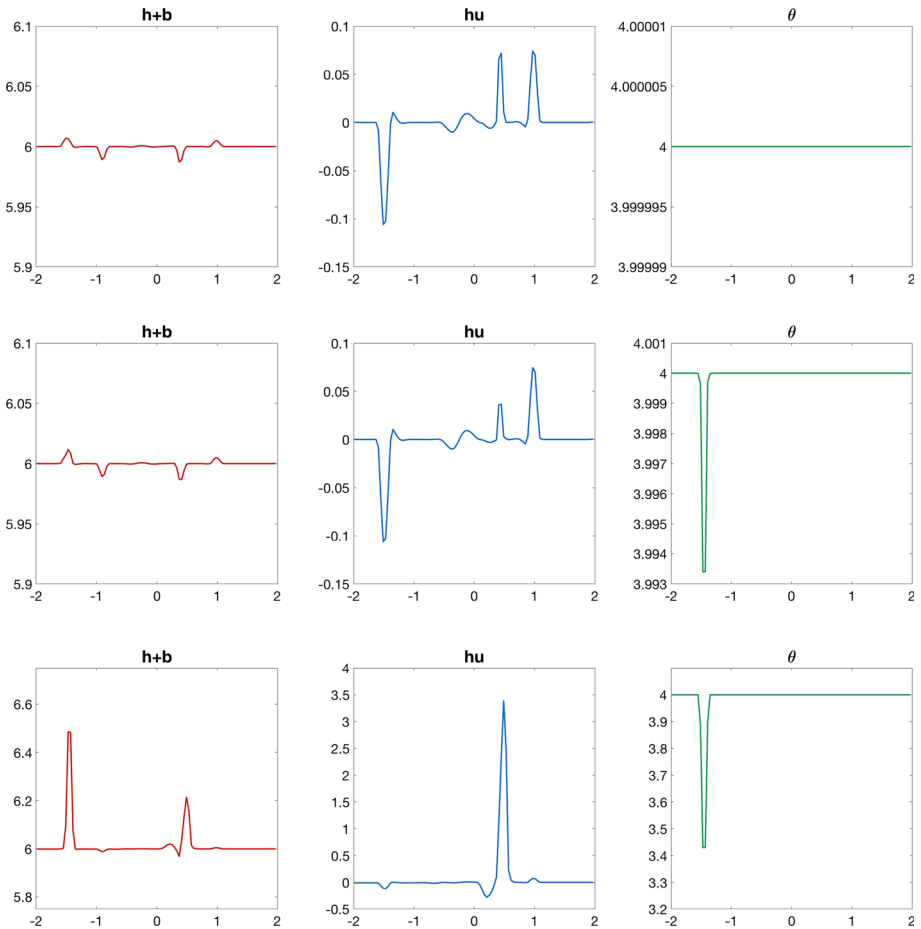
Fig. 9 Solutions of perturbation tests (3.6) (top row), (3.7) (middle row), and (3.8) (bottom row), using the traditional DG method. In all cases, the traditional DG scheme doesn't handle perturbations as well as the still-water well-balanced scheme. The larger the perturbation, the closer the results of the traditional DG methods are to the well-balanced method

3.4 Tests for Riemann Problems

In this subsection, we consider problems that contain discontinuities in the initial conditions, known as Riemann problems or dam break problems for the shallow water equations.

First, we consider the dam break problem in the computational domain $[-200, 400]$ with the initial conditions

$$(h, u, \theta)(x, 0) = \begin{cases} (5, 0, 20), & \text{when } x < 0, \\ (10, 40, 5), & \text{when } x \geq 0. \end{cases} \tag{3.9}$$

The bottom function is given as $b(x) = 0$ and we employ transmissive boundary conditions. This example is computed using the still-water well-balanced DG method with a uniform mesh of 200 cells. Figure 10 displays the numerical results at times $t = 1, 2,$ and 3, and the solutions are captured well by our methods.
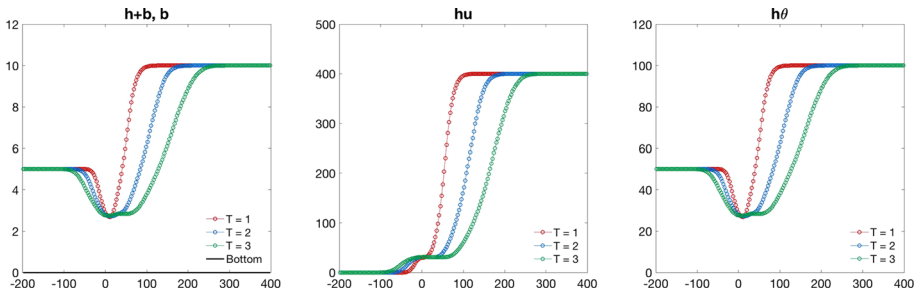
Fig. 10 Numerical solutions of the well-balanced DG methods for (3.9) at various times with 200 uniform cells
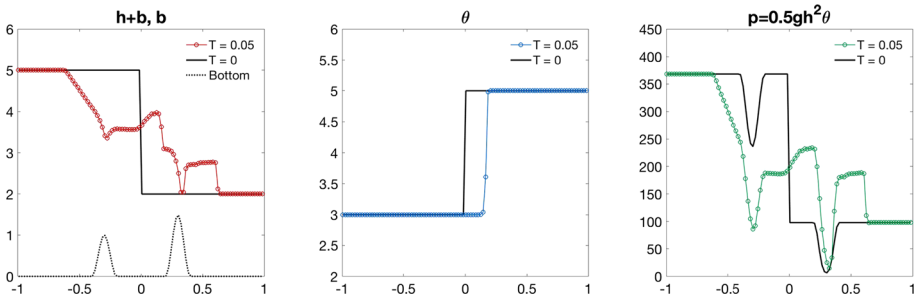
Fig. 11 Initial conditions and numerical solutions of test (3.11) at time $t = 0.05$ using 200 uniform cells. The water surface $h + b$, bottom topography b, potential temperature field θ, and pressure $p = \frac{1}{2} g h^2 \theta$ are plotted. The result for θ is a horizontal translation of the initial condition

Next, we look at the dam break problem over a non-flat bottom. We define the bottom topography on the domain $[-1, 1]$ to include two bumps:

$$b(x) = \begin{cases} 0.5 \cos{(10\pi (x + 0.3))} + 1, & \text{when } -0.4 \le x \le -0.2, \\ 0.75 \cos{(10\pi (x - 0.3))} + 1, & \text{when } 0.2 \le x \le 0.4, \\ 0, & \text{otherwise.} \end{cases} \tag{3.10}$$

The initial conditions are defined as:

$$(h, u, \theta)(x, 0) = \begin{cases} (5, 0, 3), & \text{when } x < 0, \\ (2, 0, 5), & \text{when } x \ge 0. \end{cases} \tag{3.11}$$

We test the problem until time 0.05. Figure 11 shows the results at the final time, compared to the initial conditions. We see that the potential temperature field at the final time is a horizontal translation of the initial condition. The proposed DG methods can capture the discontinuity very well even on a coarse mesh of 200 uniform cells.

4 Moving-Water Well-Balanced DG Methods

The objective of this section is to present well-balanced methods which maintain the general moving steady state (1.8). Compared with the still-water equilibrium, the moving-water steady state is more complex, therefore, special care is provided to the recovery of the

well-balanced states, the source term approximation, and the construction of well-balanced numerical fluxes. We also show how the well-balanced methods for the general moving steady state can be extended to the isobaric (1.6) and constant water height (1.7) steady states.

4.1 Numerical Initial Conditions

Recovery of the well-balanced states from the numerical initial conditions in the piecewise polynomial space $\mathbb{V}_\tau^k$ can be a challenging task. Usually, the initial conditions of the modal DG method are taken to be the L^2 projection of the true initial conditions U_0, which works well for the lake-at-rest still-water preserving methods. However, the projected polynomial, denoted as $U_{0,\tau}$, may not be in the equilibrium state when the moving-water equilibrium is considered. As a result, the cell boundary values $U_{\tau,j+\frac{1}{2}}^\pm$ may not be in equilibrium. This is problematic because the cell boundary values are used to compute the numerical fluxes and thus increases the difficulty in designing a well-balanced scheme.

This difficulty has been observed in [30] in which well-balanced methods were designed for the shallow water equations with moving-water equilibrium state. It was resolved there by defining the well-balanced states as the solutions of nonlinear equations and then solving them using Newton's method, which could be complicated. In this paper, we propose a different and much simpler method to define the numerical initial conditions and to recover the well-balanced states, thanks to the flexibility of the DG methods.

The initial conditions of the DG method should be polynomials that approximate the exact solutions with enough accuracy. Thus we introduce a new projection (known as the Radau projection) of the initial condition by defining $\mathbb{P}_\tau \omega$ to be a projection of ω into $\mathbb{V}_\tau^k$, such that

$$\int_{I_j} \mathbb{P}_\tau \omega v \, dx = \int_{I_j} \omega v \, dx \tag{4.1}$$

for any $v \in P^{k-1}$ on I_j, and

$$(\mathbb{P}_\tau \omega)\left(x_{j+\frac{1}{2}}^-\right) = \omega\left(x_{j+\frac{1}{2}}\right), \tag{4.2}$$

at the right boundary value $x_{j+\frac{1}{2}}$ of the cell I_j. The polynomial $\mathbb{P}_\tau \omega$ for each cell I_j can be determined by solving a local linear algebra problem of the size $(k+1) \times (k+1)$ derived from the discretized versions of (4.1) and (4.2).

We define the projection of the initial condition $U_{0,\tau}$ and the projection of the bottom function $b_\tau(x)$ to be

$$U_{0,\tau}(x) = \mathbb{P}_\tau U_0(x), \quad b_\tau(x) = \mathbb{P}_\tau b(x), \tag{4.3}$$

and it can be shown that

$$U_{0,\tau}\left(x_{j+\frac{1}{2}}^-\right) = U_0\left(x_{j+\frac{1}{2}}\right), \quad b_\tau\left(x_{j+\frac{1}{2}}^-\right) = b\left(x_{j+\frac{1}{2}}\right), \quad \text{for all } j. \tag{4.4}$$

Thus, at the right boundary point of each cell I_j, the equilibrium states (1.8) are recovered using the piecewise polynomial projections of the exact solutions, i.e.,

$$\left(\frac{u_\tau^2}{2} + g\theta_\tau(h_\tau + b_\tau)\right)\left(x_{j+\frac{1}{2}}^-\right) = constant, \quad \text{for all } j.$$

Notice that the numerical initial condition is only in perfect equilibrium at the right boundary point of each cell.

Remark 4.1 The choice of the projection $\mathbb{P}_\tau$ is not unique. Instead of requiring the projected function match the original function at the right end point $x_{j+\frac{1}{2}}$ as in (4.2), we could choose any other point in the cell I_j, except the center x_j. Such projection with the choice of x_j has been presented in [18]. However, we noticed that projection is only optimal when the polynomial degree k is even, and it is suboptimal when k is odd.

4.2 Conservative and Equilibrium Variables

We denote the moving-water equilibrium variables from (1.8) as:

$$V = \begin{pmatrix} E \\ m \\ \theta \end{pmatrix} = \begin{pmatrix} \frac{u^2}{2} + g\theta(h+b) \\ hu \\ \theta \end{pmatrix}, \tag{4.5}$$

which become constants at the steady state (1.8). It is necessary to transform the conservative variables U into equilibrium variables V, and vice versa in the process of maintaining the well-balanced property. Given U and the bottom function b, the equilibrium variables can be easily computed, and we denote it by $V = V(U, b)$. On the other hand, suppose V and the bottom function b are given, we can evaluate $U = U(V, b)$ in the following way. Let us rewrite E as

$$E = \frac{m^2}{2h^2} + g\theta(h+b), \tag{4.6}$$

which leads to the cubic polynomial

$$\frac{m^2}{2} + (g\theta b - E)h^2 + (g\theta)h^3 = 0. \tag{4.7}$$

To recover the water height h, we find the correct root of this cubic polynomial. Three roots of a cubic polynomial can be found analytically. If the polynomial returns three real-valued roots, one of them is negative, and the other two correspond to the subsonic and supersonic cases. We choose $h(V, b)$ as the root that is closest to $h_\tau(\hat{x}_i)$, where $\hat{x}_i$ is either a quadrature point or a cell-boundary value. In the other case when the polynomial has one real-valued root and two complex-valued roots, the only real-valued root is negative and we choose $h(V, b)$ to be the real part of the complex roots. Once h is obtained, m and $h\theta$ can be easily recovered from V.

Next, we propose to decompose the solution U_τ, into the reference equilibrium state U_τ^e and the fluctuation part U_τ^f, with the expectation that U_τ^f reduces to 0 at the moving-water equilibrium (1.8). Note that this decomposition will be computed not only for the initial conditions, but also at each time step. In each computational cell I_j, the equilibrium state $U_\tau^e(x)$ can be computed from the constant equilibrium variables

$$\hat{V}_j = \begin{pmatrix} \hat{E}_j \\ \hat{m}_j \\ \hat{\theta}_j \end{pmatrix} = \begin{pmatrix} E_\tau\left(x_{j+\frac{1}{2}}^-\right) \\ m_\tau\left(x_{j+\frac{1}{2}}^-\right) \\ \theta_\tau\left(x_{j+\frac{1}{2}}^-\right) \end{pmatrix}, \tag{4.8}$$

and the bottom function b_τ in the form of

$$U_\tau^e(x) = \begin{pmatrix} h_\tau^e(x) \\ (hu)_\tau^e(x) \\ (h\theta)_\tau^e(x) \end{pmatrix} := \mathbb{P}_\tau U(\hat{V}_j, b_\tau). \tag{4.9}$$

Unlike the still-water case in (2.11), the functions $U(\hat{V}_j, b_\tau)$ may not be piecewise polynomials as a result of the nonlinear mapping, even though $\hat{V}_j$ is constant and $b_\tau \in \mathbb{V}_\tau^k$. Therefore, the same projection $\mathbb{P}_\tau$ is used to project them into the DG space $\mathbb{V}_\tau^k$. Lastly, we can decompose the numerical solution U_τ as follows:

$$U_\tau = U_\tau^e + U_\tau^f, \tag{4.10}$$

where $U_\tau^f = U_\tau - U_\tau^e \in \mathbb{V}_\tau^k$. If the initial condition $U_0(x)$ is in the moving-water equilibrium (1.8), the reference equilibrium state U_τ^e (constructed in the way above) is identical to the solution U_τ, and therefore $U_\tau^f = 0$.

4.3 Well-Balanced Numerical Fluxes

The semi-discrete moving-water well-balanced DG method for (2.2) is defined as follows: we seek the DG solution U_τ satisfying

$$\int_{I_j} \partial_t(U_\tau)v \, dx - \int_{I_j} f(U_\tau)\partial_x v \, dx + \hat{f}_{j+\frac{1}{2}}^l v_{j+\frac{1}{2}}^- - \hat{f}_{j-\frac{1}{2}}^r v_{j-\frac{1}{2}}^+ = \int_{I_j} S(U_\tau, b_\tau)v \, dx, \tag{4.11}$$

for any test function $v(x) \in \mathbb{V}_\tau^k$. In order to determine the well-balanced numerical fluxes, we extend the hydrostatic reconstruction approach presented in Sect. 2.2 for the still-water equilibrium. After computing the boundary values $U_{\tau, j+\frac{1}{2}}^\pm$ at the time step t^n, we again set

$$b_{\tau, j\pm\frac{1}{2}}^* = \max\left(b_{\tau, j\pm\frac{1}{2}}^+, b_{\tau, j\pm\frac{1}{2}}^-\right). \tag{4.12}$$

However, other generalizations of the hydrostatic reconstruction could also be used. Next, the height function at the cell interface can be redefined as:

$$
\begin{aligned}
h_{\tau, j+\frac{1}{2}}^{*,-} &= \max\left(0, h\left(\hat{V}_j, b_{\tau, j+\frac{1}{2}}^*\right) + h_{\tau, j+\frac{1}{2}}^{f,-}\right), \\
h_{\tau, j+\frac{1}{2}}^{*,+} &= \max\left(0, h\left(\hat{V}_{j+1}, b_{\tau, j+\frac{1}{2}}^*\right) + h_{\tau, j+\frac{1}{2}}^{f,+}\right),
\end{aligned}
\tag{4.13}
$$

where the values $\hat{V}_j$ are given in (4.8) and h_τ^f is given in (4.10). This results in following updated boundary values of U:

$$U_{\tau, j+\frac{1}{2}}^{*,\pm} = \begin{pmatrix} h_{\tau, j+\frac{1}{2}}^{*,\pm} \\ m_{\tau, j+\frac{1}{2}}^\pm \\ h_{\tau, j+\frac{1}{2}}^{*,\pm} \theta_{\tau, j+\frac{1}{2}}^\pm \end{pmatrix}. \tag{4.14}$$

Finally, the well-balanced numerical fluxes can be computed:

$$
\begin{aligned}
\hat{f}_{j+\frac{1}{2}}^l &= F\left(U_{\tau, j+\frac{1}{2}}^{*,-}, U_{\tau, j+\frac{1}{2}}^{*,+}\right) + f\left(U_{\tau, j+\frac{1}{2}}^-\right) - f\left(U_{\tau, j+\frac{1}{2}}^{*,-}\right), \\
\hat{f}_{j-\frac{1}{2}}^r &= F\left(U_{\tau, j-\frac{1}{2}}^{*,-}, U_{\tau, j-\frac{1}{2}}^{*,+}\right) + f\left(U_{\tau, j-\frac{1}{2}}^+\right) - f\left(U_{\tau, j-\frac{1}{2}}^{*,+}\right),
\end{aligned}
\tag{4.15}
$$

where $F(a, b)$ is a consistent numerical flux, such as the Lax–Friedrichs flux defined in (2.6). Again, at the moving-water equilibrium (1.8), we have $\hat{V}_j = constant$ and $h_\tau^f = 0$, therefore, $h_{\tau,j+\frac{1}{2}}^{*,+} = h_{\tau,j+\frac{1}{2}}^{*,-}$ following the definition in (4.13). This leads to the continuity of U_τ^* at cell interfaces, i.e. $U_{\tau,j+\frac{1}{2}}^{*,+} = U_{\tau,j+\frac{1}{2}}^{*,-}$. As a result, we can show that

$$\hat{f}_{j+\frac{1}{2}}^l = f\left(U_{j+\frac{1}{2}}^-\right), \quad \hat{f}_{j-\frac{1}{2}}^r = f\left(U_{j-\frac{1}{2}}^+\right), \tag{4.16}$$

due to the consistency of the numerical flux $F(a, b)$.

Remark 4.2 The recovery of h from the equilibrium variable V via solving a cubic polynomial is needed twice at each time step, namely in (4.9) and (4.13) described above. Numerically, the cubic polynomial computations allot for approximately 10–12% of total computational time. One could further reduce the computational cost if redefining the variable b^* in (4.12) to

$$b_{\tau,j\pm\frac{1}{2}}^* = b_{\tau,j\pm\frac{1}{2}}^-, \tag{4.17}$$

which matches the definition of the Radau projection in (4.2). Therefore, $h(\hat{V}_j, b_{\tau,j+\frac{1}{2}}^*)$ reduces to $h_{\tau,j+\frac{1}{2}}^-$, and the updated cell boundary value $h^{*,\pm}$ in (4.13) becomes

$$h_{\tau,j+\frac{1}{2}}^{*,-} = \max\left(0, h_{\tau,j+\frac{1}{2}}^- + h_{\tau,j+\frac{1}{2}}^{f,-}\right), \quad h_{\tau,j+\frac{1}{2}}^{*,+} = \max\left(0, h_{\tau,j+\frac{1}{2}}^- + h_{\tau,j+\frac{1}{2}}^{f,+}\right), \tag{4.18}$$

which now does not involve the step to solve the cubic polynomial.

4.4 The Source Term Approximation

To maintain the well-balanced property, we introduce the following way to decompose the source term, by directly extending the idea in Sect. 2.3 for the still-water equilibrium. We first decompose the source term into the equilibrium and fluctuation parts

$$\int S(U_\tau, b_\tau)v\, dx = \int S(U_\tau^e, b_\tau)v\, dx + \int S(U_\tau^f, b_\tau)v\, dx. \tag{4.19}$$

As before, we use a quadrature rule to compute the second term on the right hand side. For the first term, we notice that the equality

$$\int_{I_j} S\left(U(\hat{V}_j, b_\tau), b_\tau\right)v\, dx = -\int_{I_j} f\left(U(\hat{V}_j, b_\tau)\right)v_x\, dx + f\left(U(\hat{V}_j, b_\tau)\left(x_{j+\frac{1}{2}}^-\right)\right)v_{j+\frac{1}{2}}^-$$
$$- f\left(U(\hat{V}_j, b_\tau)\left(x_{j-\frac{1}{2}}^+\right)\right)v_{j-\frac{1}{2}}^+, \tag{4.20}$$

holds when the exact integration is used, since $U(\hat{V}_j, b_\tau)$ is the equilibrium solution in the cell I_j. In (4.9), U_τ^e is defined as the projection of $U(\hat{V}_j, b_\tau)$ with approximation error $O(\tau^{k+1})$. Taking this error into consideration, the equation (4.20) becomes

$$\int_{I_j} S(U_\tau^e, b_\tau)v\, dx + O\left(\tau^{k+1}\right) = -\int_{I_j} f(U_\tau^e)v_x\, dx + f\left(U_{\tau,j+\frac{1}{2}}^{e,-}\right)v_{j+\frac{1}{2}}^-$$
$$- f\left(U_{\tau,j-\frac{1}{2}}^{e,+}\right)v_{j-\frac{1}{2}}^+, \tag{4.21}$$

in which the integrals can also be computed via quadrature rule with the same error $O(\tau^{k+1})$. Unlike the still-water case in Sect. 2.3, the term $f(U_\tau^e)$ is no longer a polynomial, even though U_τ^e is, and we cannot compute these integrals exactly with a sufficiently accuracy quadrature rule. To this end, the source term can be evaluated using the following form:

$$\int_{I_j} S(U_\tau, b_\tau) v \, dx = -\int_{I_j} f(U_\tau^e) v_x \, dx + f\left(U_{\tau,j+\frac{1}{2}}^{e,-}\right) v_{j+\frac{1}{2}}^-$$
$$-f\left(U_{\tau,j-\frac{1}{2}}^{e,+}\right) v_{j-\frac{1}{2}}^+ + \int_{I_j} S\left(U_\tau^f, b_\tau\right) v \, dx. \qquad (4.22)$$

4.5 Slope Limiter

When the solution contains discontinuities, a slope limiter procedure may be necessary after each inner stage of the Runge–Kutta time stepping procedure. We use the standard total variation bounded (TVB) slope limiter [27] presented below. The TVB corrected minmod function is defined by

$$\tilde{m}(a_1, \ldots, a_l) = \begin{cases} a_1, & \text{if } |a_1| \leq M\tau^2, \\ m(a_1, \ldots, a_l), & \text{otherwise,} \end{cases} \qquad (4.23)$$

where M is the TVB parameter, and the minmod function $m(a_1, \ldots, a_l)$ is defined as:

$$m(a_1, \ldots, a_l) = \begin{cases} s \min(|a_1|, \ldots, |a_l|), & \text{if } s = \text{sign}(a_1) = \cdots = \text{sign}(a_l), \\ 0, & \text{otherwise .} \end{cases} \qquad (4.24)$$

The slope limiter procedure involves two steps. First, one must check if any limiting in needed in a specific cell. If the corrected minmod function returns the first argument, i.e.,

$$\tilde{m}\left(U_\tau\left(x_{j+\frac{1}{2}}^-\right) - \bar{U}_{\tau,j}, \bar{U}_{\tau,j} - \bar{U}_{\tau,j-1}, \bar{U}_{\tau,j+1} - \bar{U}_{\tau,j}\right) = U_\tau\left(x_{j+\frac{1}{2}}^-\right) - \bar{U}_{\tau,j},$$
$$\tilde{m}\left(\bar{U}_{\tau,j} - U_\tau\left(x_{j-\frac{1}{2}}^+\right), \bar{U}_{\tau,j} - \bar{U}_{\tau,j-1}, \bar{U}_{\tau,j+1} - \bar{U}_{\tau,j}\right) = \bar{U}_{\tau,j} - U_\tau\left(x_{j-\frac{1}{2}}^+\right), \qquad (4.25)$$

with $\bar{U}_{\tau,j}$ standing for the cell average of U_τ in the cell I_j, the limiting is not necessary in this cell. Otherwise, we need to apply the limiter to all the variables in that cell, which is the second step of the slope limiter procedure. We define the modified cell boundary values to be

$$U_\tau^{(\text{mod})}\left(x_{j+\frac{1}{2}}^-\right) = \bar{U}_{\tau,j} + \tilde{m}\left(U_\tau\left(x_{j+\frac{1}{2}}^-\right) - \bar{U}_{\tau,j}, \bar{U}_{\tau,j} - \bar{U}_{\tau,j-1}, \bar{U}_{\tau,j+1} - \bar{U}_{\tau,j}\right),$$
$$U_\tau^{(\text{mod})}\left(x_{j-\frac{1}{2}}^+\right) = \bar{U}_{\tau,j} - \tilde{m}\left(\bar{U}_{\tau,j} - U_\tau\left(x_{j-\frac{1}{2}}^+\right), \bar{U}_{\tau,j} - \bar{U}_{\tau,j-1}, \bar{U}_{\tau,j+1} - \bar{U}_{\tau,j}\right). \qquad (4.26)$$

A P^2 polynomial that preserves the original cell average in I_j can then be recovered from the updated cell boundary values (4.26) and the cell average $\bar{U}_{\tau,j}$.

This limiting procedure may not preserve the moving-water equilibrium state (1.8). Therefore, to maintain the well-balanced state when using the slope limiter, we perform the first step (4.25) to determine if limiting is necessary in each cell, based on the fluctuation part of the variables U_τ^f. If limiting is required in a specific cell, the slope limiting procedure is performed on the conservation variables U_τ. If the steady state solution is reached, the fluctuation part satisfies $U_\tau^f = 0$, hence no TVB limiter is needed in any cell. Therefore the well-balanced property will not be affected by the limiter procedure. Unlike in [30], we

cannot use the equilibrium variable V_τ in the first step (4.25), due to the possibility of the cell average $\bar{V}_\tau$ not being in equilibrium even at the moving-water steady state.

4.6 Well-Balanced Property

Proposition 2 *The proposed DG scheme (4.11) for the Ripa system (1.1), paired with numerical fluxes (4.15) and source term approximation (4.22), is well-balanced for the smooth moving-water equilibrium (1.8).*

Proof Suppose the initial data are moving-water steady state equilibria. The special projection $\mathbb{P}_\tau$ ensures that the equilibrium state is maintained at the cell boundary $x_{j+1/2}^-$ for all j for the numerical initial conditions. Therefore, from the definition of (4.8), we have $\hat{V}_j = constant$ for all j. This implies the equilibrium part U_τ^e, computed from $\hat{V}_j$ and b_τ in (4.9), is equivalent to U_τ and that $U_\tau^f = 0$. The source term approximation (4.22) becomes

$$\int_{I_j} S(U_\tau, b_\tau) v \, dx = -\int_{I_j} f(U_\tau) v_x \, dx + f\left(U_{\tau,j+\frac{1}{2}}^-\right) v_{j+\frac{1}{2}}^- - f\left(U_{\tau,j-\frac{1}{2}}^+\right) v_{j-\frac{1}{2}}^+ \quad (4.27)$$

At the same time, since $U_\tau^f = 0$, the modified cell boundary values satisfy

$$U_{\tau,j+\frac{1}{2}}^{*,-} = \begin{pmatrix} \max\left(0, h\left(\hat{V}_j, b_{j+\frac{1}{2}}^*\right)\right) \\ \hat{m}_{j+\frac{1}{2}}^- \\ \max\left(0, h\left(\hat{V}_j, b_{j+\frac{1}{2}}^*\right)\right)\hat{\theta}_{j+\frac{1}{2}}^- \end{pmatrix} = \begin{pmatrix} \max\left(0, h\left(\hat{V}_{j+1}, b_{j+\frac{1}{2}}^*\right)\right) \\ \hat{m}_{j+\frac{1}{2}}^+ \\ \max\left(0, h\left(\hat{V}_{j+1}, b_{j+\frac{1}{2}}^*\right)\right)\hat{\theta}_{j+\frac{1}{2}}^+ \end{pmatrix} = U_{\tau,j+\frac{1}{2}}^{*,+}.$$

$$(4.28)$$

Due to the consistency of the Lax–Friedrichs flux and (4.28), it can be shown that

$$\hat{f}_{j+\frac{1}{2}}^l = f\left(U_{\tau,j+\frac{1}{2}}^-\right), \quad \hat{f}_{j-\frac{1}{2}}^r = f\left(U_{\tau,j-\frac{1}{2}}^+\right), \quad (4.29)$$

and the flux terms at the left hand side of (4.11) reduce to

$$-\int_{I_j} f(U_\tau)\partial_x v \, dx + f\left(U_{\tau,j+\frac{1}{2}}^-\right) v_{j+\frac{1}{2}}^- - f\left(U_{\tau,j-\frac{1}{2}}^+\right) v_{j-\frac{1}{2}}^+.$$

It thus follows that the flux terms exactly balance the source term approximation, and the well-balanced property is proven. □

We finish this section with some remarks about the moving-water equilibrium preserving well-balanced RKDG method.

Remark 4.3 When the bottom topography is flat (i.e., $b(x) = constant\ C$), the traditional DG methods are recovered from our well-balanced DG scheme, that is, the source term approximation reduces to 0 exactly and the left and right numerical fluxes reduce to the original fluxes. First of all, in each cell I_j, $\hat{V}_j$ defined in (4.8) is a scalar number. When $b(x) = C$ is a constant, the value of $h(\hat{V}_j, C)$ is also a constant which does not depend on x within each cell I_j. The same observation holds for $U_\tau^e(x) \equiv \mathbb{P}_\tau U(\hat{V}_j, C)$. Therefore, we have

$$\int_{I_j} S\left(U_\tau^e, b_\tau\right) v \, dx = -\int_{I_j} f\left(U_\tau^e\right) v_x \, dx + f\left(U_{\tau,j+\frac{1}{2}}^{e,-}\right) v_{j+\frac{1}{2}}^- - f\left(U_{\tau,j-\frac{1}{2}}^{e,+}\right) v_{j-\frac{1}{2}}^+ = 0.$$

Also, the numerical integral $\int_{I_j} S\left(U_\tau^f, b_\tau\right) v \, dx = 0$, since $b_\tau(x) = C$ leads to $(b_\tau)_x = 0$. Together, this implies the source term approximation presented in (4.22) is zero.

Second, we show that the well-balanced numerical flux reduces to the standard DG flux. Note that, when $b(x) = C$ is a constant, $b^*_{\tau, j \pm \frac{1}{2}}$ defined by (4.12) or (4.17) is also the same constant C. Therefore,

$$h^{*,-}_{\tau, j+\frac{1}{2}} = \max\left(0, h(\hat{V}_j, C) + h^{f,-}_{\tau, j+\frac{1}{2}}\right) = \max\left(0, h^{e,-}_{\tau, j+\frac{1}{2}} + h^{f,-}_{\tau, j+\frac{1}{2}}\right) = h^-_{\tau, j+\frac{1}{2}}.$$

(4.30)

Similarly, it can be shown that $h^{*,+}_{\tau, j+\frac{1}{2}} = h^+_{\tau, j+\frac{1}{2}}$ and more generally that $U^{*,\pm}_{\tau, j+\frac{1}{2}} = U^\pm_{\tau, j+\frac{1}{2}}$. Therefore the left and right numerical fluxes defined in (4.15) reduce to the original DG fluxes: $\hat{f}^l_{j+\frac{1}{2}} = \hat{f}_{j+\frac{1}{2}}$, $\hat{f}^r_{j-\frac{1}{2}} = \hat{f}_{j-\frac{1}{2}}$.

Remark 4.4 Our well-balanced methods are designed to preserve the moving-water equilibrium (1.8). When applied to the still-water steady state (1.5), which is a special case of the moving-water equilibrium with $m = 0$, they should automatically preserve this simpler equilibrium. In fact, they reduce to the same still-water well-balanced methods presented in Sect. 2 with the exception of the choice of projection.

4.7 Well-Balanced Methods for the Constant Water Height and Isobaric Equilibria

The proposed framework to balance the moving-water equilibrium can also be extended to preserve the constant water height steady state (1.7) and the isobaric steady state (1.6) of the Ripa model. For each given equilibrium, one well-balanced method to balance this equilibrium can be designed, but we cannot combine these into a unified well-balanced method. Below, we will discuss how to design such scheme briefly with some necessary details provided.

First, let's consider the constant water height steady state solution (1.7). Let the equilibrium variables be denoted

$$\hat{V}_j = \begin{pmatrix} \hat{h}_j \\ \hat{m}_j \\ \hat{L}_j \end{pmatrix} = \begin{pmatrix} h_\tau\left(x^-_{j+\frac{1}{2}}\right) \\ (hu)_\tau\left(x^-_{j+\frac{1}{2}}\right) \\ \left(b_\tau + \frac{1}{2} h_\tau \ln \theta_\tau\right)\left(x^-_{j+\frac{1}{2}}\right) \end{pmatrix},$$

(4.31)

then the equilibrium parts can be determined as follows:

$$U^e_{\tau, j}(x) = \begin{pmatrix} h^e_{\tau, j}(x) \\ (hu)^e_{\tau, j}(x) \\ (h\theta)^e_{\tau, j}(x) \end{pmatrix} = \begin{pmatrix} \hat{h}_j \\ \hat{m}_j \\ \hat{h}_j \mathbb{P}_\tau\left(\exp\left(\frac{2}{\hat{h}_j}(\hat{L}_j - b_\tau(x))\right)\right) \end{pmatrix},$$

(4.32)

where $\mathbb{P}_\tau$ is the same Radau projection described in (4.1) and (4.2). The fluctuation part U_τ^f is again determined by the decomposition $U_\tau = U_\tau^e + U_\tau^f$. Next, we determine the modified cell interface values as

$$(h\theta)^{*,-}_{\tau,j+\frac{1}{2}} = \max\left(0, \hat{h}_j \exp\left(\frac{2}{\hat{h}_j}\left(\hat{L}_j - b^*_{\tau,j+\frac{1}{2}}\right)\right) + (h\theta)^{f,-}_{j+\frac{1}{2}}\right),$$

$$(h\theta)^{*,+}_{\tau,j+\frac{1}{2}} = \max\left(0, \hat{h}_{j+1} \exp\left(\frac{2}{\hat{h}_{j+1}}\left(\hat{L}_{j+1} - b^*_{\tau,j+\frac{1}{2}}\right)\right) + (h\theta)^{f,+}_{j+\frac{1}{2}}\right),$$

(4.33)

where $b^*_{\tau,j+\frac{1}{2}} = \max\left(b^+_{\tau,j+\frac{1}{2}}, b^-_{\tau,j+\frac{1}{2}}\right)$. We let $h^{*,\pm}_{\tau,j+\frac{1}{2}} = h^{\pm}_{\tau,j+\frac{1}{2}}$ and $(hu)^{*,\pm}_{\tau,j+\frac{1}{2}} = (hu)^{\pm}_{\tau,j+\frac{1}{2}}$. Then at the steady state we have $U^{*,-}_{\tau,j+\frac{1}{2}} = U^{*,+}_{\tau,j+\frac{1}{2}}$ since h, hu are both constant and $U^f_\tau = 0$ at the steady state. Lastly, let the choices of left and right fluxes as well as the source term approximation be the same as for the moving-water schemes. The numerical methods designed in this way can be shown to preserve the constant water height state exactly.

Secondly, the isobaric steady state solution (1.6) is considered. Let us denote the equilibrium variables as

$$\hat{V}_j = \begin{pmatrix} \hat{m}_j \\ \hat{S}_j \end{pmatrix} = \begin{pmatrix} (hu)_\tau\left(x^-_{j+\frac{1}{2}}\right) \\ h_\tau(h\theta)_\tau\left(x^-_{j+\frac{1}{2}}\right) \end{pmatrix},$$

(4.34)

then the equilibrium parts can be determined as

$$U^e_{\tau,j}(x) = \begin{pmatrix} h^e_{\tau,j}(x) \\ (hu)^e_{\tau,j}(x) \\ (h\theta)^e_{\tau,j}(x) \end{pmatrix} = \begin{pmatrix} h_{\tau,j}(x) \\ \hat{m}_j \\ \mathbb{P}_\tau\left(\frac{\hat{S}_j}{h_{\tau,j}(x)}\right) \end{pmatrix},$$

(4.35)

and the fluctuation part is defined by $U^f_\tau = U_\tau - U^e_\tau$. Now, if we let $h^*_{\tau,j+\frac{1}{2}} = h^{*,\pm}_{\tau,j+\frac{1}{2}} = \max\left(h^-_{\tau,j+\frac{1}{2}}, h^+_{\tau,j+\frac{1}{2}}\right)$ and set $(hu)^{*,\pm}_{\tau,j+\frac{1}{2}} = (hu)^{\pm}_{\tau,j+\frac{1}{2}}$, we can determine the last conservative variable as

$$(h\theta)^{*,-}_{\tau,j+\frac{1}{2}} = \max\left(0, \frac{\hat{S}_j}{h^*_{\tau,j+\frac{1}{2}}} + (h\theta)^{f,-}_{\tau,j+\frac{1}{2}}\right),$$

$$(h\theta)^{*,+}_{\tau,j+\frac{1}{2}} = \max\left(0, \frac{\hat{S}_{j+1}}{h^*_{\tau,j+\frac{1}{2}}} + (h\theta)^{f,-}_{\tau,j+\frac{1}{2}}\right).$$

(4.36)

The numerical scheme is completed by using the formulations for the source term as well as the left and right fluxes found in the moving-water scheme. It then follows that the scheme exactly preserves the isobaric steady state.

5 Numerical Tests for Moving-Water Well-Balanced Methods

In this section, we present numerical results of our moving-water well-balanced DG methods for the one-dimensional Ripa system (1.1), using the well-balanced technique described in Sect. 4. We implement our scheme using piecewise quadratic polynomials ($k = 2$) in space, paired with the third order TVD Runge–Kutta time discretization (2.9). The CFL number

Table 3 L^1 errors and orders of accuracy for the test in Sect. 5.1, using the moving-water well-balanced method

No. of cells	h		hu		$h\theta$	
	L^1 error	Order	L^1 error	Order	L^1 error	Order
25	7.3659e−04		6.7798e−03		7.8134e−04	
50	1.1235e−04	2.7129	9.0751e−04	2.9013	1.1063e−04	2.8201
100	1.5781e−05	2.8317	1.1708e−04	2.9544	1.8243e−05	2.6004
200	2.0662e−06	2.9331	1.5041e−05	2.9606	2.7879e−06	2.7101
400	2.5592e−07	3.0132	1.8865e−06	2.9951	3.8607e−07	2.8522

is again taken to be 0.1. The constant M in the TVB limiter is taken to be 0, except for the accuracy test in which no slope limiter was used. The gravitational constant g is fixed to be 9.812 m/s^2. Multiple types of numerical tests have been carried out in this section to demonstrate the capacity of our proposed moving-water well-balanced methods.

5.1 Tests for Accuracy

In this subsection, we will check the accuracy of our moving-water well-balanced scheme for smooth solutions. The same setup of the initial conditions and boundary conditions, as in Sect. 3.1, is used here. We run the numerical simulation until time $t = 0.02$, while the numerical solution is still smooth. Table 3 contains the L^1 errors and numerical orders for the moving-water well-balanced DG method. It is easy to observe that the expected high order accuracy is obtained by the proposed methods.

5.2 Tests for the Well-Balanced Property

The following tests are chosen to verify that the proposed DG methods preserve the moving-water steady states (1.8) when a non-flat bottom topography $b(x)$ exists. For these examples, the errors are calculated by comparing the numerical results to the initial conditions.

We present the test cases of both sub-critical and trans-critical flows. These tests are extensions of widely used numerical experiments for verifying the performance of numerical schemes for the shallow water equations in [19,29–31]. The bottom function is given by:

$$b(x) = \begin{cases} 0.2 - 0.05(x - 10)^2, & \text{if } 8 \leq x \leq 12, \\ 0, & \text{otherwise,} \end{cases} \tag{5.1}$$

for a channel of length 25 m. Two types of moving-water steady states solutions, corresponding to sub-critical and trans-critical flows, will be investigated below.

(a) *Sub-critical flow* The initial conditions are given by

$$\begin{cases} m = 4.42\sqrt{5} \\ E = 22.06605 \cdot 5 \\ \theta = 5 \end{cases} \tag{5.2}$$

with the boundary conditions of $m = 4.42\sqrt{5}$ at the upstream and $h = 2$ at the downstream.

Table 4 L^1 and L^∞ errors for the well-balanced tests of different moving-water equilibria, at time $t = 1$ with 200 uniform cells

Test	L^1 error			L^∞ error		
	h	hu	$h\theta$	h	hu	$h\theta$
(5.2)	3.9850e−13	6.0707e−13	4.0459e−13	1.5654e−13	4.2100e−13	1.5965e−13
(5.3)	7.2879e−14	3.0429e−13	7.2849e−14	8.0269e−14	1.8407e−13	7.6161e−14
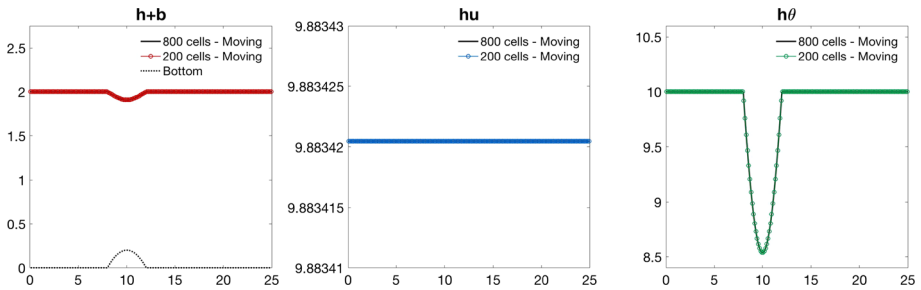
Fig. 12 Numerical solutions for sub-critical flow (5.2) at time $t = 1$ with 200 and 800 uniform cells. The steady state is preserved for both mesh sizes when the moving-water well-balanced scheme is used

(b) *Trans-critical flow* The initial conditions are given by:

$$\begin{cases} m = 1.53\sqrt{5} \\ E = 11.09098731433671 \cdot 5 \\ \theta = 5 \end{cases} \tag{5.3}$$

with the boundary conditions of $m = 1.53\sqrt{5}$ at the upstream and $h = 0.405737258401203$ at the downstream. The flow moves from subsonic to supersonic at $x = 10$, which occurs at the peak of the bottom topography function.

For both test cases, the moving-water steady state solutions should be preserved exactly. We run both cases until time the stopping time of $t = 1$, using a coarse mesh of 200 uniform cells and a finer mesh of 800 cells for comparison. The L^1 and L^∞ errors in Table 4 demonstrate the well-balanced property is maintained up to round-off error when using the moving-water preserving method. The numerical results are presented in Figs. 12 and 13. For comparison, we also compute these moving-water steady states using the still-water well-balanced methods presented in Sect. 2. Figures 14 and 15 display the difference between the numerical solution and the initial conditions. It can be seen from the plots that the moving-water steady states are not preserved by the still-water preserving method.

5.3 Tests of Small Perturbations

The tests in this subsection are selected to demonstrate that small perturbations to the moving-water steady states are well captured by the proposed moving-water well-balanced DG scheme. Similar tests have been presented in [30,35] for the shallow water equations. We will consider two perturbation sizes to the sub-critical and trans-critical moving-water steady states.
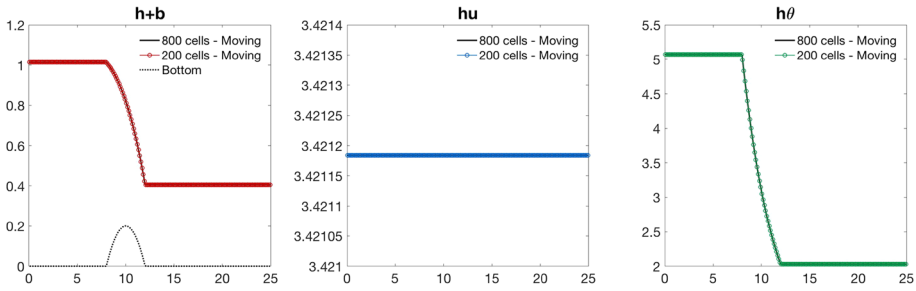
Fig. 13 Numerical solutions for trans-critical flow (5.3) at time $t = 1$ with 200 and 800 uniform cells. The steady state is preserved for both mesh sizes even with the flow changing from sub-critical to super-critical when the moving-water well-balanced scheme is implemented
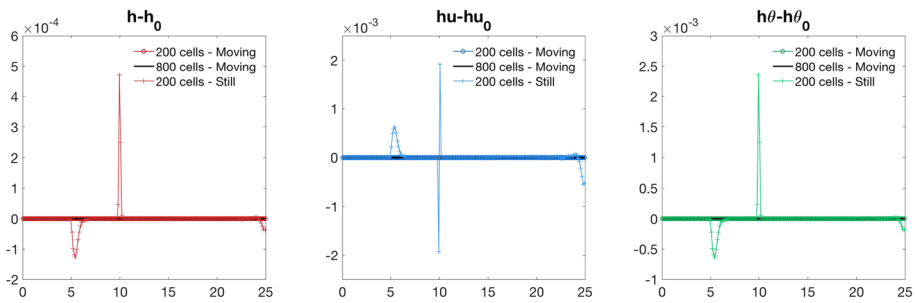
Fig. 14 The difference between the solutions $h, hu, h\theta$ for the sub-critical flow problem (5.2) at time $t = 1$ and the corresponding steady state solutions. Both the moving-water and still-water scheme results are plotted
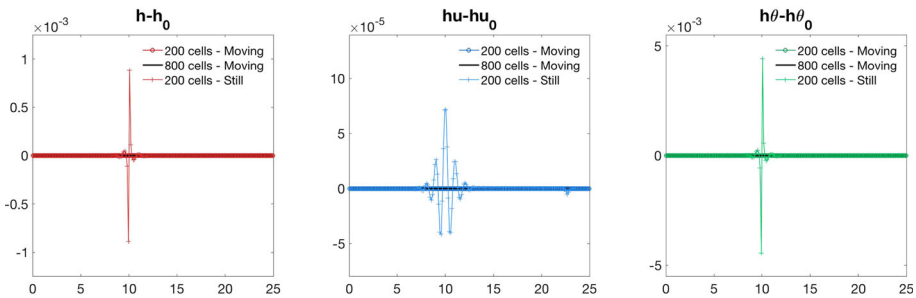
Fig. 15 The same as Fig. 14, except for the trans-critical flow problem (5.3)

The initial conditions are given by the sub-critical and trans-critical flow (5.2) and (5.3) in Sect. 5.2, with an added perturbation to h and $h\theta$ in the interval [5.75, 6.25]. That is, if we denote the moving-water steady state initial conditions in Sect. 5.2 as $\left(h_{eq}, (hu)_{eq}, (h\theta)_{eq}\right)$, the initial conditions of the perturbed tests are given by

(a) *Larger perturbation*

$$\left(h, (hu), (h\theta)\right)(x, 0) = \left(h_{eq}, (hu)_{eq}, (h\theta)_{eq}\right)(x, 0) + [0.05, 0, 0.25]_{\chi_{[5.75, 6.25]}}. \quad (5.4)$$
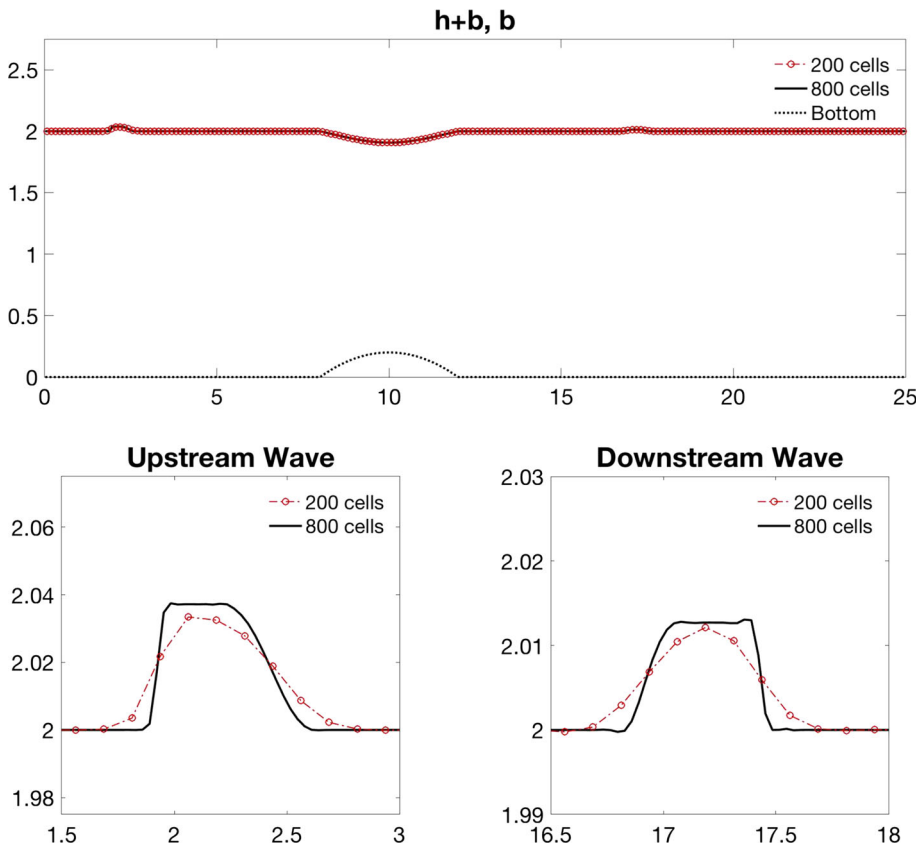
Fig. 16 Water height h of the well-balanced methods for the larger perturbation test of sub-critical flow (5.2) at time $t = 0.75$ with mesh sizes of 200 and 800 uniform cells. The bottom row contains zoomed in images of the waves of h

(b) *Smaller perturbation*

$$\big(h, (hu), (h\theta)\big)(x, 0) = \big(h_{eq}, (hu)_{eq}, (h\theta)_{eq}\big)(x, 0) + [0.0001, 0, 0.0005]_{\chi_{[5.75, 6.25]}}.$$
(5.5)

The value $\chi_{[5.75, 6.25]}$ is defined to be 1 in the region $[5.75, 6.25]$ and 0 everywhere else in the domain.

It is expected that the perturbation will split into two waves traveling in opposite directions away from their point of origin. We run the test until the stopping time of $t = 0.75$. At this time, the downstream moving wave will have passed the bump of the bottom topography function. The numerical results for the large perturbation of the sub-critical flow problem are shown in Figs. 16 and 17, where we compare the results of moving-water well-balanced DG method on mesh sizes of 200 and 800 uniform cells. One can observe that the propagation of these small perturbations is well captured by our methods, and there are no visible numerical oscillations in the solutions. We demonstrate the numerical results of the larger perturbation for the trans-critical flow problem in Figs. 18 and 19, and similar observations can be found.
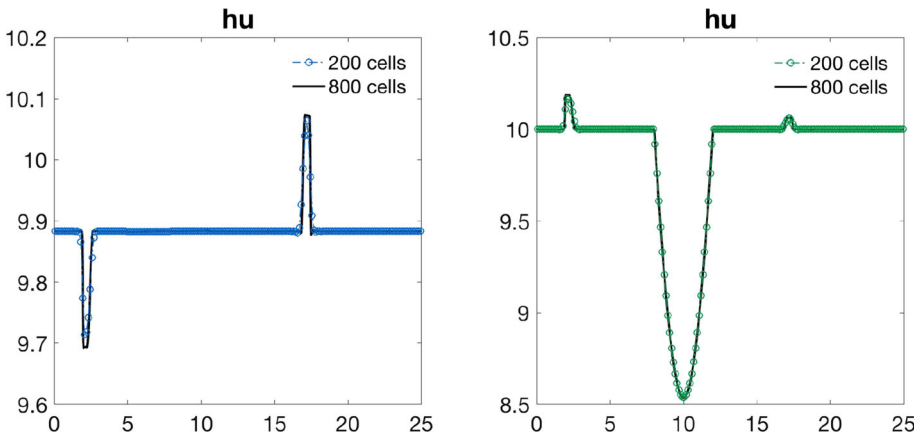
Fig. 17 Numerical solutions of hu and $h\theta$ for the larger perturbation test of sub-critical flow problem (5.2) at time $t = 0.75$ with mesh sizes of 200 and 800 uniform cells
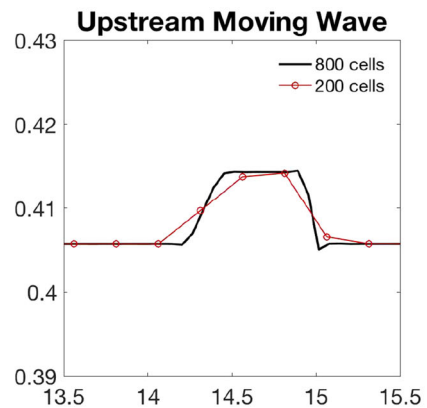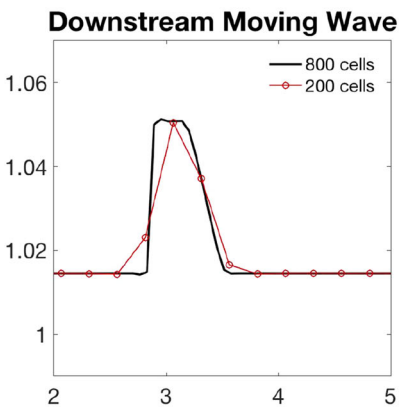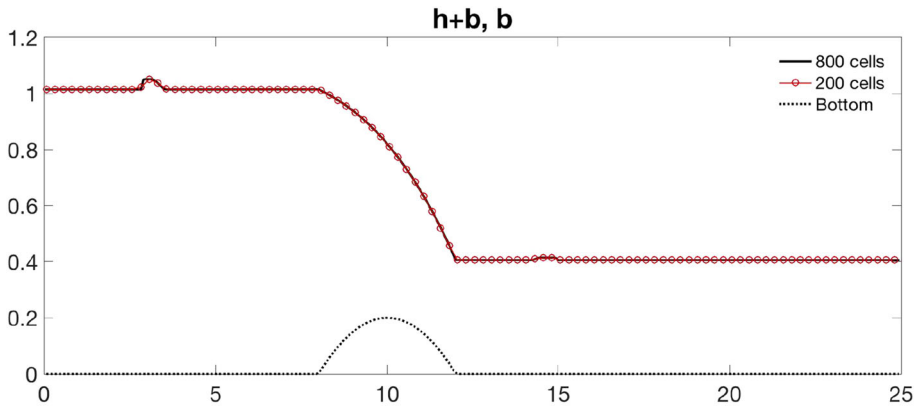
Fig. 18 Water height h of the well-balanced methods for the larger perturbation test of trans-critical flow (5.3) at time $t = 0.75$ with mesh sizes of 200 and 800 uniform cells. The bottom row contains zoomed in images of the waves of h
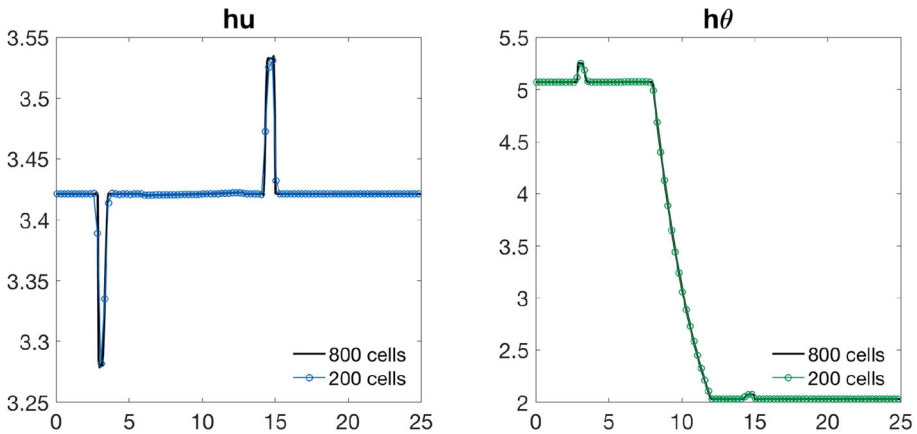
Fig. 19 Numerical solutions of hu and $h\theta$ for the larger perturbation test of trans-critical flow problem (5.3) at time $t = 0.75$ with mesh sizes of 200 and 800 uniform cells
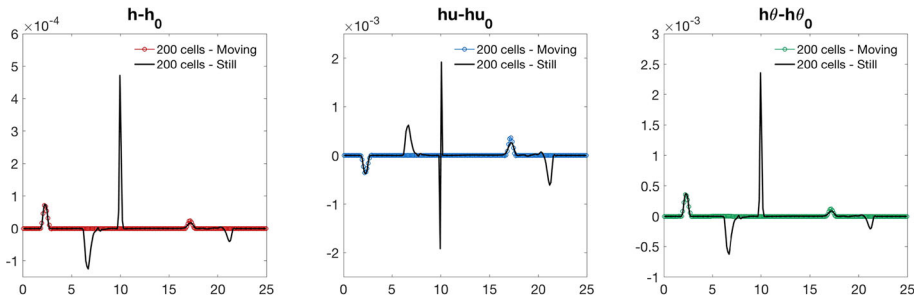
Fig. 20 The difference between the solutions h, hu, $h\theta$ for the smaller perturbation of the sub-critical flow problem (5.2) at time 0.75 and the corresponding steady state solutions. A uniform mesh of 200 cells has been used for both the still-water and moving-water schemes

Next, we present the numerical results from the smaller perturbation tests, and compare the performance of the moving-water and still-water preserving schemes on a mesh of 200 uniform cells. Figure 20 contains plots of the difference between the solutions h, hu, $h\theta$ at the final time 0.75 and the corresponding steady states for the sub-critical flow problem. It can be seen that the still-water preserving DG scheme does not handle perturbations to the moving-water steady state nearly as well as the moving-water preserving scheme. Similar results have been observed for the trans-critical flow problem, see Fig. 21. These results demonstrate the importance of moving-water preserving method in capturing the propagation of these small perturbations.

5.4 Riemann Problems

In this subsection, we consider three Riemann problems that contain discontinuities in the initial conditions, to demonstrate the performance of our proposed methods when the solutions contain discontinuity.
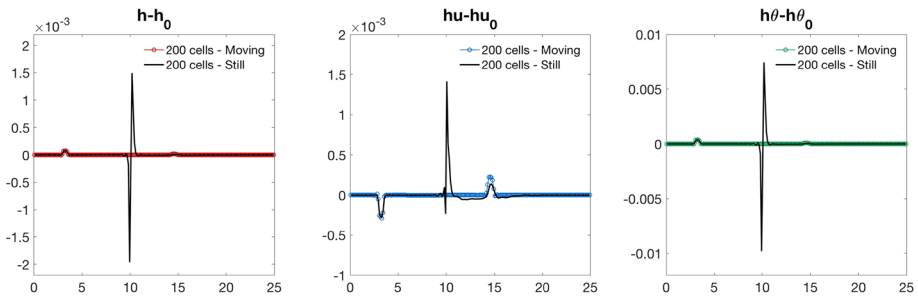
Fig. 21 The difference between the solutions $h, hu, h\theta$ for the smaller perturbation of the trans-critical flow problem (5.3) at time 0.75 and the corresponding steady state solutions. A uniform mesh of 200 cells has been used for both the still-water and moving-water schemes
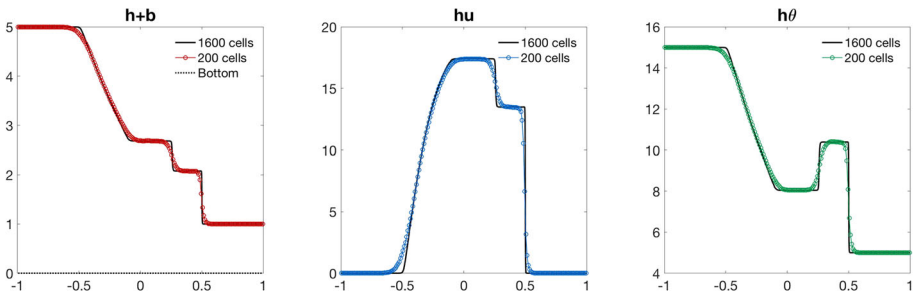
Fig. 22 Numerical solution for the Riemann problem (5.6) at time $t = 0.04$ with 200 and 1600 cells using the moving-water well-balanced method

First, we consider a problem with no initial velocity, a flat bottom ($b(x) = 0$), and the following initial conditions for $x \in [-1, 1]$:

$$h(x, 0) = \begin{cases} 5, & \text{when } x < 0, \\ 1, & \text{when } x \geq 0, \end{cases} \quad u(x, 0) = 0, \quad \theta(x, 0) = \begin{cases} 3, & \text{when } x < 0, \\ 5, & \text{when } x \geq 0. \end{cases} \quad (5.6)$$

Transmissive boundary conditions are employed for all variables. We run the simulation until time $t = 0.04$, and both shock and rarefaction waves appear in this test. Figure 22 displays the numerical results of our methods with 200 uniform cells, and we also include the numerical results of 1600 cells as the "reference" solutions for comparison. One can observe that the numerical solutions agree well with the "reference" solutions, and both the shock and rarefaction wave are captured well by the moving-water well-balanced DG methods.

Second, we consider a dam break problem over a flat bottom, in which all initial conditions are non-zero. The initial conditions in the computational domain $[-1, 1]$ are set as

$$\left(h(x, 0), u(x, 0), \theta(x, 0) \right) = \begin{cases} (2, 0.5, 1), & \text{when } |x| < 0.5, \\ (1, 0.75, 1.55), & \text{otherwise,} \end{cases} \quad (5.7)$$

with $b(x) = 0$. Transmissive boundary conditions are employed for all variables. We run the simulation until time $t = 0.075$, and six waves including both shock and rarefaction waves appear. Figure 23 displays the numerical results of our methods with 200 uniform cells, and the "reference" solutions obtained with refined 1600 uniform cells. Again, one can observe
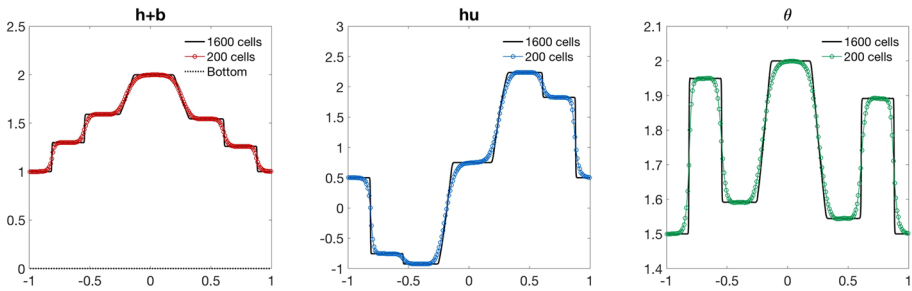
Fig. 23 Numerical solution for the Riemann problem (5.7) at time $t = 0.075$ with 200 and 1600 cells using the moving-water well-balanced method

that the numerical solutions agree well with the "reference" solutions, and all these waves are captured well by the moving-water well-balanced DG methods.

Lastly, we consider a dam break problem over a non-flat and discontinuous bottom topography. We set our computational domain to be [0, 600] in which the bottom function and initial conditions are defined as:

$$b(x) = \begin{cases} 8, & \text{when } |x - 300| < 75, \\ 0, & \text{otherwise,} \end{cases} \tag{5.8}$$

and

$$(h, u, \theta)(x, 0) = \begin{cases} (20 - b(x), 1, 10), & \text{when } x < 300, \\ (15 - b(x), 5, 5), & \text{when } x \geq 300. \end{cases} \tag{5.9}$$

Transmissive boundary conditions are employed for all variables. The simulation is ran until the stopping time $t = 3$, and the solution demonstrate a complicated structure, due to the interaction of the waves with the discontinuous bottom function. The conservative variables $(h, hu, h\theta)$ as well as velocity u, temperature θ, and pressure $p = \frac{1}{2}g\theta h^2$ are displayed in Fig. 24. The numerical results of both 200 and 1600 uniform cells are presented in these figures. We can observe that the numerical solutions agree well with the "reference" solutions. All these waves, including the shocks near $x = 375$, are captured well by the moving-water well-balanced DG methods.

6 Concluding Remarks

In this paper, well-balanced DG methods for the shallow water equations with horizontal temperature gradients, also known as the Ripa model, are designed and tested. We present two types of well-balanced methods, one for the the simpler still-water equilibrium (1.5) and the other for more complicated moving-water equilibrium (1.8), and show that the former one is a special case of the latter. We also demonstrated the same framework can be extended to design well-balanced methods for the isobaric steady state (1.6) and the constant water height steady state (1.7), with different definitions of $U_\tau^e(x)$ and $U_{\tau, j+\frac{1}{2}}^{*,\pm}$ following the equilibria to be preserved. The proposed method is an extension of the well-balanced method [30] for the shallow water equations, but with several improvements to simplify the algorithms. To achieve the well-balanced property, special attention was paid to the approximation of the source term and the construction of the numerical fluxes. Numerical examples were given
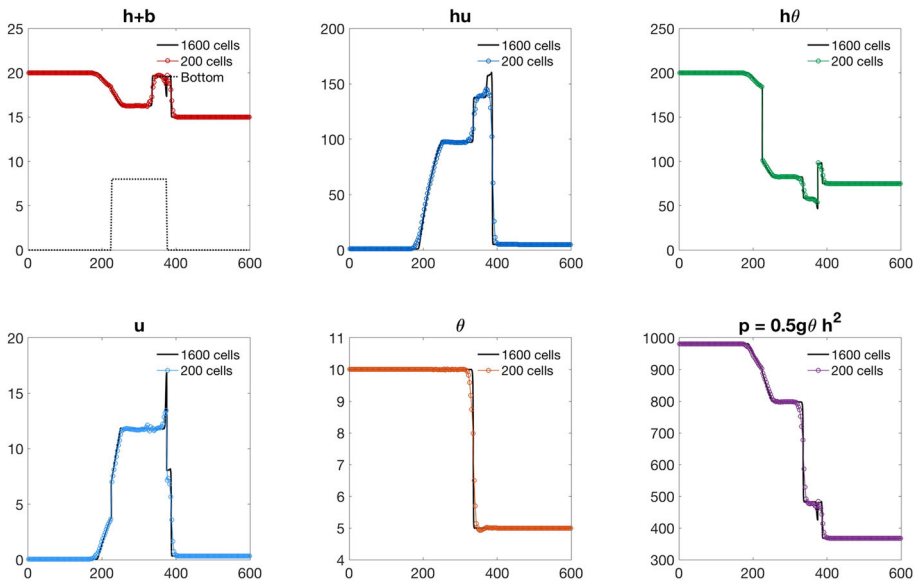
Fig. 24 Numerical solution for the Riemann problem (5.9) at time $t = 3$ with 200 and 1600 cells using the moving-water well-balanced method. Both the water surface $h + b$, momentum hu, $h\theta$, and the velocity u, θ, pressure p are shown

to demonstrate the accuracy, well-balanced property, perturbations to steady states, and non-oscillatory behavior near discontinuities. This approach is rather general and can be applied to design well-balanced methods for other hyperbolic balance laws.

References

1. Audusse, E., Bouchut, F., Bristeau, M.-O., Klein, R., Perthame, B.: A fast and stable well-balanced scheme with hydrostatic reconstruction for shallow water flows. SIAM J. Sci. Comput. **25**, 2050–2065 (2004)
2. Bermudez, A., Vazquez, M.E.: Upwind methods for hyperbolic conservation laws with source terms. Comput. Fluids **23**, 1049–1071 (1994)
3. Bouchut, F., Morales, T.: A subsonic-well-balanced reconstruction scheme for shallow water flows. SIAM J. Numer. Anal. **48**, 1733–1758 (2010)
4. Bouchut, F., Zeitlin, V.: A robust well-balanced scheme for multi-layer shallow water equations. Discrete Contin. Dyn. Syst. B **13**, 739–758 (2010)
5. Castro, M.J., López-García, J.A., Pares, C.: High order exactly well-balanced numerical methods for shallow water systems. J. Comput. Phys. **246**, 242–264 (2013)
6. Chen, G., Noelle, S.: A new hydrostatic reconstruction scheme motivated by the wet–dry front. SIAM J. Numer. Anal. **55**, 758–784 (2017)
7. Cheng, Y., Chertock, A., Herty, M., Kurganov, A., Wu, T.: A new approach for designing moving-water equilibria preserving schemes for the shallow water equations. J. Sci. Comput. **80**, 538–554 (2019)
8. Cheng, Y., Kurganov, A.: Moving-water equilibria preserving central-upwind schemes for the shallow water equations. Commun. Math. Sci. **14**, 1643–1663 (2016)
9. Chertock, A., Kurganov, A., Liu, Y.: Central-upwind schemes for the system of shallow water equations with horizontal temperature gradients. Numer. Math. **127**, 595–639 (2014)
10. Cockburn, B., Karniadakis, G., Shu, C.-W.: The development of discontinuous Galerkin methods. In: Cockburn, B., Karniadakis, G., Shu, C.-W. (eds.) Discontinuous Galerkin Methods: Theory, Computation and Applications. Lecture Notes in Computational Science and Engineering, Part I: Overview, vol. 11, pp. 3–50. Springer, Berlin (2000)

11. Dellar, P.: Common Hamiltonian structure of the shallow water equations with horizontal temperature gradients and magnetic fields. Phys. Fluids **15**, 292–297 (2003)
12. Desveaux, V., Zenk, M., Berthon, C., Klingenberg, C.: Well-balanced schemes to capture non-explicit steady states: Ripa model. Math. Comput. **85**, 1571–1602 (2016)
13. Han, X., Li, G.: Well-balanced finite difference WENO schemes for the Ripa model. Comput. Fluids **134–135**, 1–10 (2016)
14. Hernandez-Duenas, G.: A hybrid method to solve shallow water flows with horizontal density gradients. J. Sci. Comput. **73**, 753–782 (2017)
15. Kurganov, A.: Finite-volume schemes for shallow-water equations. Acta Numer. **27**, 289–351 (2018)
16. Kurganov, A., Levy, D.: Central-upwind schemes for the Saint-Venant system. Math. Model. Numer. Anal. **36**, 397–425 (2002)
17. LeVeque, R.J.: Balancing source terms and flux gradients on high-resolution Godunov methods: the quasi-steady wave-propagation algorithm. J. Comput. Phys. **146**, 346–365 (1998)
18. Li, G., Xing, Y.: Well-balanced discontinuous Galerkin methods with hydrostatic reconstruction for the Euler equations with gravitation. J. Comput. Phys. **352**, 445–462 (2018)
19. Noelle, S., Xing, Y., Shu, C.-W.: High order well-balanced finite volume WENO schemes for shallow water equation with moving water. J. Comput. Phys. **226**, 29–58 (2007)
20. Qiu, J., Khoo, B.C., Shu, C.-W.: A numerical study for the performance of the Runge–Kutta discontinuous Galerkin method based on different numerical fluxes. J. Comput. Phys. **212**(2), 540–565 (2006)
21. Ricchiuto, M., Bollermann, A.: Stabilized residual distribution for shallow water simulations. J. Comput. Phys. **228**, 1071–1115 (2009)
22. Ripa, P.: Conservation laws for primitive equations models with inhomogeneous layers. Geophys. Astrophys. Fluid Dyn. **70**, 85–111 (1993)
23. Ripa, P.: On improving a one-layer ocean model with thermodynamics. J. Fluid Mech. **303**, 16–201 (1995)
24. Russo, G.: Central schemes for conservation laws with application to shallow water equations. In: Rionero, S., Romano, G. (eds.) Trends and Applications of Mathematics to Mechanics: STAMM 2002, pp. 225–246. Springer, Berlin (2005)
25. Russo, G., Khe, A.: High order well balanced schemes for systems of balance laws. In: Hyperbolic Problems: Theory, Numerics and Applications, pp. 919–928. Proceedings of Symposia in Applied Mathematics 67, Part 2, American Mathematics Society, Providence, RI (2009)
26. Sanchez-Linares, C., Morales de Luna, T., Castro, M.J.: A HLLC scheme for Ripa model. Appl. Math. Comput. **272**, 369–384 (2016)
27. Shu, C.-W.: TVB uniformly high-order schemes for conservation laws. Math. Comput. **49**, 105–121 (1987)
28. Touma, R., Klingenberg, C.: Well-balanced central finite volume methods for the Ripa system. Appl. Numer. Math. **97**, 42–68 (2015)
29. Vazquez-Cendon, M.E.: Improved treatment of source terms in upwind schemes for the shallow water equations in channels with irregular geometry. J. Comput. Phys. **148**, 497–526 (1999)
30. Xing, Y.: Exactly well-balanced discontinuous Galerkin methods for the shallow water equations with moving water equilibrium. J. Comput. Phys. **257**, 536–553 (2014)
31. Xing, Y., Shu, C.-W.: High order finite difference WENO schemes with the exact conservation property for the shallow water equations. J. Comput. Phys. **208**, 206–227 (2005)
32. Xing, Y., Shu, C.-W.: High order well-balanced finite volume WENO schemes and discontinuous Galerkin methods for a class of hyperbolic systems with source terms. J. Comput. Phys. **214**, 567–598 (2006)
33. Xing, Y., Shu, C.-W.: A new approach of high order well-balanced finite volume WENO schemes and discontinuous Galerkin methods for a class of hyperbolic systems with source terms. Commun. Comput. Phys. **1**, 100–134 (2006)
34. Xing, Y., Shu, C.-W.: A survey of high order schemes for the shallow water equations. J. Math. Study **47**, 221–249 (2014)
35. Xing, Y., Shu, C.-W., Noelle, S.: On the advantage of well-balanced schemes for moving-water equilibria of the shallow water equations. J. Sci. Comput. **48**, 339–349 (2011)
36. Xing, Y., Zhang, X., Shu, C.-W.: Positivity-preserving high order well-balanced discontinuous Galerkin methods for the shallow water equations. Adv. Water Resour. **33**, 1476–1493 (2010)